Building carbon-free colloidal nanocrystal assemblies with plasma rocessing

by

Pratyasha Mohapatra

A thesis submitted to the graduate faculty

in partial fulfillment of the requirements for the degree of

MASTER OF SCIENCE

Major: Materials Science and Engineering

Program of Study Committee:
Ludovico Cademartiri, Major Professor
Martin Thuo
Matthew Panthani
Xiaoli Tan

The student author, whose presentation of the scholarship herein was approved by the program of study committee, is solely responsible for the content of this thesis. The Graduate College will ensure this thesis is globally accessible and will not permit alterations after a degree is conferred.

Iowa State University

Ames, Iowa

2017

TABLE OF CONTENTS

ACKNOWLEDGMENTS

I would like to thank my Advisor, Dr. Ludovico Cademartiri, for providing me with the opportunity, guidance and motivation to work on this research. I would also take the opportunity to thank my committee members Dr. Martin Thuo, Dr. Matthew Panthani, and Dr. Xiaoli Tan for their encouragement and support for my research.

In addition, I would also like to thank my friends and colleagues, Pratyush, Souvik, Bin, Xinchun, Santosh, Julia, Lin, Kara, Oskar and Yichao for helping and supporting me, whenever needed, throughout the period of my research. I would like to extend my gratitude to Jonathan, Prof. Emily Smith, Fabian, Tiago, Wai, and the staff at CIS, MRC, MARL, MSE department, for their cooperation and help for the timely progress of the research.

ABSTRACT

Removing the organic fraction from hybrid nanostructures is a crucial step in most bottom-up materials fabrication approaches. It is usually assumed that calcination is an effective solution, especially for thin films. This assumption has led to its application in thousands of papers. We here test this assumption using a relevant and highly controlled model system consisting of thin films of ligand-capped ZrO2 nanocrystals. Consistently with carbonization, while Raman characterization fails to detect the ligands after calcination, Electron Backscattered Spectroscopy characterization demonstrates that ~20% of the original carbons are left behind even after calcination at 800C for 12hrs. By comparison plasma processing successfully removes the ligands. Our growth kinetic analysis shows that the leftover carbon can significantly affect interfacial properties.

We then employ plasma processing to remove ligands from synthesized colloidal silicon nanoparticle (nc-Si) assemblies to form crack free thin films. We also compare the Reactive Ion etching characteristics of these plasma processed thin films with single crystalline silicon (sc-Si). The ligand free nc-Si thin films etch a rate twice as fast as sc-Si. The faster etch rates are expected owing to the porous structure of the colloidal nanostructure assemblies compared to sc-Si.

CHAPTER 1. GENERAL INTRODUCTION

The applicability of a material is greatly controlled by its material properties, which in turn depend on the structure and composition. We continuously strive for improved applications, but it is unachievable without adequately engineering the material composition. In order to be able to best engineer the properties of a material, gaining a control over its microsctructure is very important i.e: grain size, shape, composition, orientation and grain boundary composition. Nanomaterials are structures that range from a few nanometers (nm) to less than 100 nm in size. Nanostructured materials offer a plethora of properties that are often novel, better, and unachievable from their bulk counterparts. The methods of fabricating nanostructures can be broadly classified into top down and bottom up approaches. Top down techniques for nano-structured material synthesis are mostly based on nucleation from melt and may be followed by different grain refinement techniques [1]. But, these techniques can only control the average number of nuclei formed and not the nucleation sites, because of which the size and shape of the individual grains cannot be controlled. [2,3]. On the other hand, bottom up approaches with nanoparticles involve controlled synthesis of each grain independently and then assembling them together to form the final structure. It provides a high level of control on the shape, composition, size of individual particles and therefore on the final material properties of the structure [1]. Figure 1 shows different compositions (a-d) and shapes (e-h) of nanoparticles that can synthesized and used as building blocks for nanostructured materials in bottom up approached. The improved control over the nanostructure can be seen in Figure 1j that shows nearly uniform grain shape and size as compared to the varying grain sizes formed from top down techniques (fig 1i).

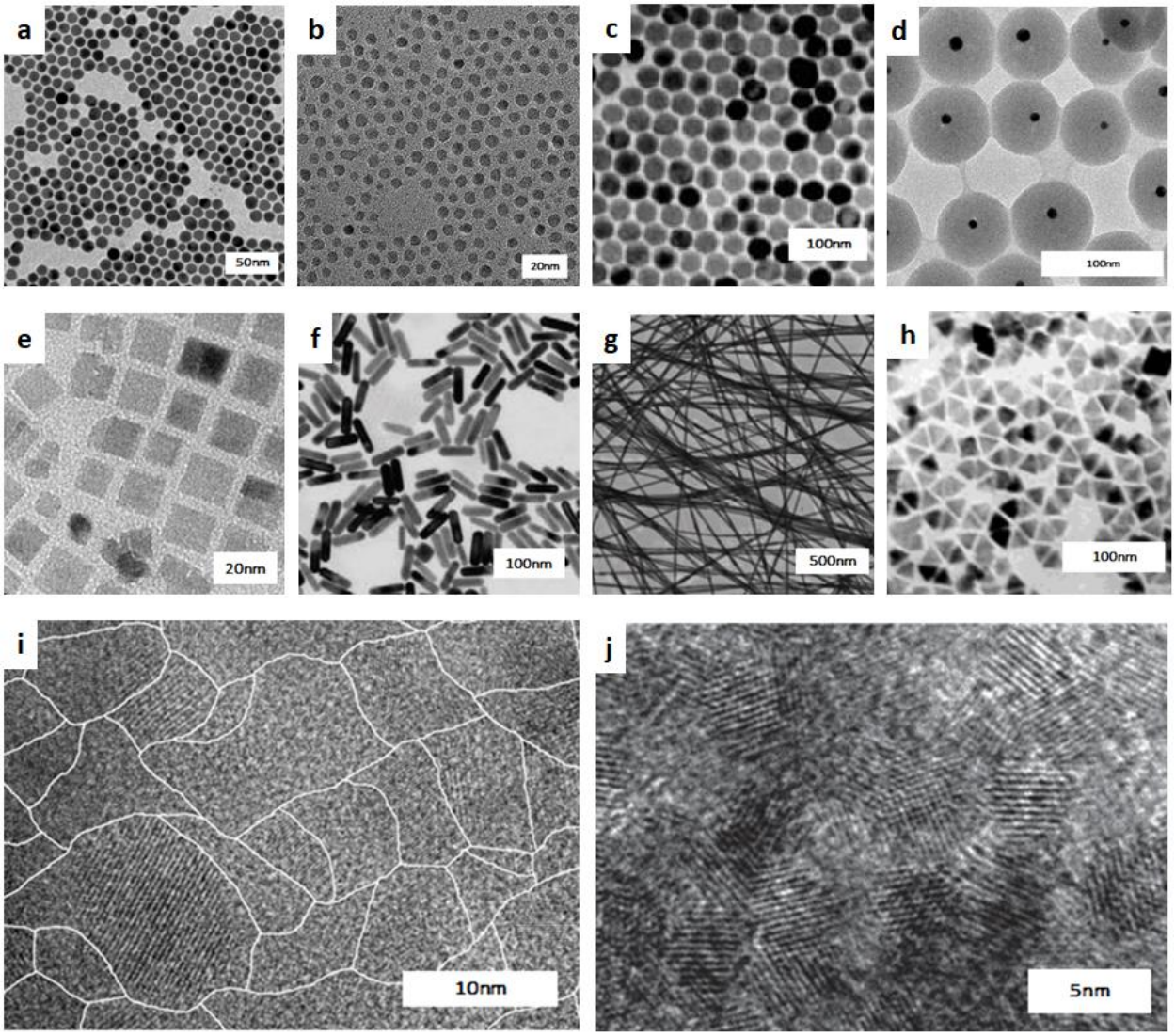

Figure 1. TEM micrographs of nanoparticles (nps) of different compositions (a) Cu nps [4] (b) InN nps [5] (c) Fe_3O_4 nps [6] (d) silica coated Au nps [7]; different shapes (e) TiO_2 nps [8] (f) Au nanorods [9] (g) Te_xSe_y@Se core-shell nanowires [10] (h) Co_3O_4 nps [6]; (i) nanostructure from top down technique [3] and (j) nanostructure from colloidal nanoparticles [11]

1.1 Colloidal Nanoparticle Assemblies

Colloidal nanoparticles are an effective building block for materials manufacturing. In colloidal nanoparticles, the organic ligand shell that coordinates the surface of the nanoparticles can control their size, prevent their agglomeration, and solvate them in suitable solvents, which facilitates the processing of these materials as liquid solutions (spin coating, dip casting, etc.).

Colloidal Nanoparticle Assembly (CNA) thin films are deposited from colloidal dispersions of colloidal nanoparticles capped with organic ligands. These organic molecules typically coordinate ~1/3 of the available metal sites on the surface. This large amount of ligands leads to CNAs in which the concentration of carbon is ~24 at% [11]. This large amount of carbon can be detrimental to the properties of materials obtained from CNAs like:

- Inorganic carbon-free interfaces are important for bio-separation, catalysis etc. to ensure sufficient clean surface available for target molecules [12, 13]
- Charge transport in energy applications may be hampered as the conducting nanoparticles are separated by ligands, like, PbSe nanoparticle arrays [14] and PbS CNA thin films [11] were found to be completely insulating in the presence of a ligand shell.
- Ligands can block light in photo synthetic application there by reducing the efficiency [15]
- Full densification of any material built from colloids necessitates removal of all carbon from the solvent and ligands

1.2 Methods of Ligand Removal from CNAs

One of the most common methods to remove ligands is by direct calcination. Calcination has been used for removing the organic ligand shells from colloidal nanoparticle assemblies to produce ligand free surfaces for different applications [16,17]. Calcination removes the carbon in CNA thin films by oxidizing the ligands at high temperatures in air or oxygen. The process is used to (i) remove the organic fraction of the material [16,17] (ii) increase the mechanical stability by sintering the adjacent grains together [12], and (iii) crystallize the structure.

But the process is delicate for many reasons:

- At the calcination temperatures, the carbon in the ligand may yield a composite structure resulting from the incomplete combustion of the carbon, leading to carbonization. The composite structure would not have properties of the phase pure inorganic nanoparticle species. The properties like electric conductivity, density would be altered in unpredictable ways. Furthermore, the amorphous carbon phases that would result from such carbonization would be remarkably difficult to properly characterize due to the lack of sensitivity of most characterization techniques to carbon, especially within a material. For example, ZnO thin films show remnants of carbon from the organic precursors after a calcination treatment at 300^{o}C and 700^{o}C for 10 mins [18], Au nanoparticle assemblies show incomplete carbon removal ever after calcination at 400^{o}C [13]. Thus, this process does not produce a phase pure material and affects the material properties.
- The oxygen in the atmosphere can react with the surface of the nanoparticles, altering their chemistry and properties, especially in the case of metals, chalcogenides, pnictides and oxides of partially oxidized metals (e.g. Fe_3O_4, VO_2). The removal of organic components of CdTe thin films is carried out at 300^{o}C in nitrogen atmosphere [19]. The presence of oxygen

in the atmosphere (as in case of air) can cause CdTe to react with oxygen forming Te oxides. Silver nanoparticles also show evidence of oxidation at 200^{o}C to form oxides [20]

- In addition to the above, high temperatures may also lead to growth in the nanoparticle size, thus influencing the size dependent properties. The temperature of calcination is high enough to cause surface diffusion of atoms between the adjoining nanoparticle surfaces. The resulting sintering of the nanoparticles would compromise the size distribution of the grains and the homogeneity of their shape. [12,13,21,22]. CdTe thin films sinter at temperature as low as 240^{o}C, which is below the general calcination temperature. The particle size increases from 2.8nm at room temperature to 18 nm at 300^{o}C. At this temperature, the carbon is not completely removed. In the best case, the resulting carbon concentration is 23 at.%. [19] This carbon is attributed to decomposition products from the ligand, trapped in the films. Metal nanoparticles also show a grain growth at lower temperature around 150 – 200^{o}C [20,16]
- The high temperatures involved in the calcination process can decompose the ligands, and evolve a large amount of volatile species, leading to cracking as a result of mechanical stresses associated with volume loss. Silver nanoparticle thin films exceeding 450nm thickness, crack when annealed even at low temperatures of 150^{o}C. [16] This was attributed to inhomogeneous distribution of stress during annealing due to solvent evaporation.

Due to the above problems associated with the calcination, efforts have been continuously made to devise different methods to remove the organic ligands effectively in CNAs without hampering their structure and functionality. Some of the methods that have been utilized are by using solvent stripping method, chemical treatment, UV-ozone treatment [22,23], fast thermal treatment [24] or plasma processing.

Chemical oxidation by ozone processing [25]:

Self-assembled monolayers (SAMs) of Au nanoparticles with ligands shells are exposed to dilute ozone which oxidizes the ligand shell. The SAMs are then washed in nanopore water to wash away the oxidized ligands. However,

- The process does not remove all the ligands as only a part of the ligands is oxidized and washed away, while almost 47% of the ligands remain unchanged. [25]
- The oxidation occurs preferentially only on the top surface of the SAMs. The following water wash only removes a part of the oxidized ligands.
- The process is a wet system and water washing may not be suitable for all nanoparticles.

UV -ozone treatment:

Samples are irradiated with UV light of wavelengths 185 -257nm where the 185 nm UV generates ozone as it interacts with oxygen molecules. The UV and ozone simultaneously oxidize the organic ligands to form CO_2 and water [26]. But,

- The process shows evidence of oxidation of the nanoparticles (Pt oxidized in ozone)
- Not all of the carbon is not removed. (Aliphatic chains are removed first but carbon – nitrogen bonds, ammonium cations are difficult to remove)

Solvent extraction: .

Different solvents like water (hot ~ 90^{o}C), ethanol, etc. are used to wash nanoparticle assemblies which help to wash away the organic ligands. [13]

- Solvent extraction is generally effective for loosely bound ligands.
- Very few ligands are usually removed (~20%) after 1 hr of solvent wash [13].

- While some solvent extraction processes are not followed by calcination, they still result in grain growth (in Au particles) and incomplete carbon removal.
- Furthermore, the use of a liquid to remove the ligands tends to cause large capillary stresses in the material which can cause the films to crack.

Fast thermal treatment:

Nanoparticle assemblies (like Pt) [24] are subjected to high temperatures (300^{o}C-700^{o}C) for a very short time period (30 – 60s) in static air. The high temperatures cause the calcination of the organic ligands and the short time period prevents excessive grain growth. [24]

- The authors claimed complete removal of the carbon on the basis of the disappearance of the C-H peak in FT-IR.

Most of these procedures prioritize controlling the grain growth and the complete removal of carbon with high functionality are not achieved together.

Nanocrystal Plasma Polymerization (NPP):

NPP is an alternative technique that was introduced by us and employs low temperature plasmas for the complete removal of the organic ligand shells in colloidal nanoparticle structures without grain growth [27]. Plasma processing has been previously used commercially for surface modification, surface cleaning, deposition and chemical treatment.

1.3 What are Plasmas

Plasmas are highly ionized gas phases produced by applying an electric current to a dielectric gas [28]. A plasma may consist of electrons, positive or negative ions (depending on

the gas species), radicals, neutral atoms and molecules [29], excited species, and high energy radiation [30]. In nature, plasma is created during electric glow discharge (like in lightnings) or in very high temperature conditions (like in stars where the temperature is in the range of 10^4K) [20], when the kinetic energy of the particles is so high, that their collisions cause dissociations of molecules and the ionization of the gas species. In a laboratory, plasma is produced by generating an oscillating RF (13.56 MHz) or microwave electric field across a gas by magnetic induction or capacitive plates, at different pressures (few mTorr to atmospheric pressures). The electrons accelerated due the electric field, have elastic and inelastic collisions with the neutral atoms and form a sustained plasma. The process parameters to be controlled are:

- Plasma power
- Feed gas
- Pressure
- Flowrate

Mechanism of plasma formation

Primary electrons are produced due to the application of the electric field. These primary electrons are accelerated in the presence of the electric field and possess a high kinetic energy. The high energy electrons transfer energy to neutral atoms or molecules by collision. These collisions knock out secondary electrons from the neutral species causing them to ionize and become accelerated by the external field. The secondary electrons are also accelerated and collide with other gas atoms to further continue the ionization process finally resulting in a mass of sustained plasma. There are cases where the energy transferred by the accelerated electron is

not sufficient to ionize the gas atom. The energy transferred in this inelastic collisions excites an electron within the neutral species, causing them to be in an excited state. This excited state can relax by emitting photons. The wavelength of the generated energy radiation depends on the energy difference between the two energy levels and can be very high. The radiations (generally Vacuum Ultra-Violet (VUV) and Ultra-Violet (UV)) can break chemical bonds in molecules [31], further facilitating the ionization process in plasma. Some of the positive and negative species may even recombine to give a neutral species. The collisions, ionization, dissociations, excitation and recombination reactions [32] occur simultaneously to generate a sustained plasma. The different mechanisms involved in the plasma generation are shown below [30]:

i. Ionization: $M + e^- \rightarrow M^+ + 2e^-$ [$He + e^- \rightarrow He^+ + 2e^-$]

ii. Dissociation: $B_2 + e^- \rightarrow B^- + B$

iii. Excitation: $M + e^- \rightarrow M^* + 2e^-$

iv. De-excitation: $M^* \rightarrow M + hv$ (radiations)

v. Recombination: $M^+ + e^- \rightarrow M$, $M^+ + B^- \rightarrow M + B$

In NPP approach, plasmas are used to selectively etch the organic ligands of the CNA [16] by interacting with the exposed material surface using different mechanisms like:

- Bond cleavage – the collisions of the high energy species, or the radiations (VUV, UV) may cause scission of the organic molecular bonds to form smaller volatile species
- Chemical reaction – the active species in the plasma may chemically react with the material surface to give different reaction products
- Plasma polymerization and re-deposition – the volatile byproducts produced may polymerize in the plasma and re-deposit on the material surface

- Sputtering – when species are knocked out from the surface of the material to either leave the system as volatiles or deposit back on the surface

Nanoparticle Plasma polymerization is attractive for processing CNAs because:

i. It conserves the size, shape and composition related properties [17] – the plasma operates at temperatures that are close room temperature conditions and do not generally cause grain growth.
ii. It reduces the carbon concentration to very low levels - reported to decrease the carbon concentration from about and 23.9 at% in the deposited ZrO_2 CNA thin films to as low as about 1 at% [20]
iii. It produces crack free CNA thin films if the structure and thickness of the CNA are appropriately controlled (disordered arrays thinner than ~450nm) [16]

In spite of the advantages, there remain some issues associated with Plasma polymerization:

i. Oxygen and air plasma polymerization can lead to oxygen implantation or surface oxidation as in the case of chalcogenide nanoparticles [21]
ii. The processing takes comparatively long processing times. Though preliminary results show complete carbon removal at low time periods (nearly 6 hours) on optimization of the plasma process parameters.

1.4 Scope of the Work

Here in this work, we here compare the structural and chemical effects of calcination and plasma processing on CNAs of ZrO_2 nanoparticles. We find that, compared to plasma

processing, calcination does not fully remove the organic fraction of the CNA but rather leaves behind a substantial amount of it in the form of black carbon. The removal of ligands is incomplete for temperatures ranging from 300^{o}C to 800^{o}C and for exposures lasting 1 to 12 hrs. The concentration profile of the leftover carbon indicates that plasma processing removes carbon much more effectively than even high temperature calcination. We discuss the reason for the difference in the performance of the two approaches in terms of mass transport limitations. We find that the diffusion of gases inside the pores of the thin films do not limit the carbon removal process. This finding suggests that most materials chemistry approaches requiring the ubiquitous conversion of hybrid nanostructures (e.g., block-copolymer-templated mesoporous materials, aerogels, sol-gel coatings, inverse opals) to an inorganic crystalline phase by calcination yield composites rather than single phase materials. Especially troubling is that the spurious phase (black carbon) is one of the hardest to detect reliably and quantitatively.

In chapter 2, we then use plasma processing for ligand removal from colloidal silicon nanoparticle assemblies to form crack free, smooth nanocrystalline Si (nc-Si) thin films. These nc-Si thin films are synthesized from size controlled colloidal silicon nanoparticles. We discuss the effects of process parameters on the film quality and ways to overcome processing bottle necks to form smooth nc-Si films of varying thicknesses. We finally compare the etching rates of our plasma processed nc-Si thin films with single crystal thin films and find our nc-Si films to have a higher etch rate possibly due to the porosity in the films.

1.5 References

1. Whitesides, G.M.; Kriebel, J.K.; Mayers, B.T. Springer. 2005, 217–39
2. Moriarty, P. Reports on Progress in Physics. 2001, 64, 297–381
3. Hughes D. A.; Hansen N. Phys. Rev. Lett.112, 2014, 135504
4. Aissa, M. A. B.; Tremblay, B.; Andrieux-Ledier, A.; Maisonhaute, E.; Raouafi, N.; Courty A. Nanoscale, 2015, 7, 3189
5. Chen, Z.; Li, Y.; Cao, C.; Zhao, S.; Fathololoumi, S.; Mi, Z.; Xu, X. J.Am.Chem.Soc. 2012, 134, 780 − 783
6. Jana, N. R.; Chen, Y.; Peng, X. Chem. Mater. 2004, 16, 3931-3935
7. Han, Y.; Jiang, J.; Lee, S. S.; Ying J. Y. Langmuir 2008, 24, 5842-5848
8. Gordon, T. R.; Cargnello, M.; Paik, T.; Mangolini, F.; Weber, R. T.; Fornasiero, P.; Murray, C. B. J. Am. Chem. Soc. 2012, 134, 6751-6761.
9. Huang, X.; El-Sayed, M. A. Journal of Advanced Research 2010 ,1, 13–28
10. Yang, Y.; Wang, K.; Liang, H. W.; Liu, G. Q.; Feng, M.; Xu, L.; Liu, J. W.; Wang, J. L.; Yu, S. H. Sci. Adv. 2015;1:e1500714
11. Shaw, S.; Yuan, B.; Tian, X. C.; Miller, K. J.; Cote, B. M.; Colaux, J. L.; Migliori, A.; Panthani, M. G.; Cademartiri, L. Adv. Mater. 2016, 28, 8892-8899
12. Lu, Z.; Yin, Y. Chem. Soc. Rev., 2012, 41, 6874–6887
13. Lopez-Sanchez, J. A.; Dimitratos, N.; Hammond, C.; Brett, G. L.; Kesavan, L.; White, S.; Miedziak, P.; Tiruvalam, R.; Jenkins, R. L.; Carley, A. F.; Knight, D.; Kiely, C. J.; Hutchings, G. J. Nat. Chem. 2011, 3, 551
14. Talapin, D. V.; Murray, C. B. Science 2005, 310, 86

15. Lu, Z.; Duan, J.; He, L.; Hu Y.; Yin, Y. Anal. Chem., 2010, 82, 7249.

16. Lu, Z.; Ye, M.; Li, N.; Zhong W.; Yin, Y. Angew. Chem., Int. Ed., 2010, 49, 1862

17. Zhang, Q.; Joo, J. B.; Lu, Z.; Dahl, M.; Oliveira, D.; Ye, M.; Yin, Y. Nano Res., 2011, 4, 103

18. Petersen, J.; Brimont, C.; Gallart, M.; Schmerber, G; Gilliot, P.; Ulhaq-Bouillet, C.; Rehspringer, J. L.; Colis, S.; Becker, C.; Slaoui, A.; Dinia, A. J. Appl. Phys. 2010, 107, 123522

19. Pehnt, M.; Schilz, D.; Curtis, C.J.; Ginley, D.S. Mat. Res. Soc. Symp. Proc. Vol. 382, 1995

20. Babapour, A.; Akhavan, O.; Azimirad, R.; Moshfegh, A. Z. Nanotechnology 2006, 17, 763

21. Han, L.; Shan, Z.; Chen, D. H.; Yu, X. J.; Yang, P. Y.; Tu, B.; Zhao, D. Y. J. Colloid Interface Sci., 2008, 318, 315

22. Worley, C. G.; Linton, R. W. J. Vac. Sci. Technol., A 1995, 13, 2281–2284.

23. King, D. E. J. Vac. Sci. Technol., A 1995, 13, 1247–1253

24. Cargnello, M.; Chen, C.; Diroll, B. T.; Doan-Nguyen, V. V.; Gorte, R. J.; Murray, C. B. J. Am. Chem. Soc. 2015, 137, 6906-6911

25. Elliott, E. W.; Glover, R. D.; Hutchison, J. E. ACS Nano 2015, 9, 3050

26. Aliaga, C.; Park, J. Y.; Yamada, Y.; Lee, H. S.; Tsung, C. K.; Yang, P.; Somorjai, G. A. J. Phys. Chem. C 2009, 113, 6150

27. Shaw, S.; Colaux, J. L.; Hay, J. L.; Peiris, F. C.; Cademartiri, L. Adv. Mater. 2016, 28, 8900-8905

28. Yasuda, H. Academic Press Inc.: Orlando, FL, 1985

29. Inagaki, N. Technomic Publishing Comapny, Inc., Lancaster, PA, 1996

30. Os, M. T. Surface modification by plasma polymerization: film deposition, tailoring of surface properties and biocompatibility, Universiteit Twente, 2000

31. Uchida, S.; Takashima, S.; Hori, M.; Fukasawa, M; Ohshima, K.; Nagahata, K.; Tatsumi, T. Journal of Applied Physics 2008, 103, 073303

32. Chan, C. M. Polymer surface modification and characterization, Hanser/Gardner Publications, Inc., Cincinnatti, OH, 1994

CHAPTER 2. DOES CALCINATION REMOVE ALL CARBON FROM NANOCRYSTAL SUPERLATTICES?

Modified from a paper to be published in Nature Communications, 2017

Pratyasha Mohapatra[1], Santosh Shaw[1], Bin Yuan[2], Jonathan Bobbit[3], Emily Smith[3], Fabian Naab[4], Tiago Fiorini da Silva[5], Xinchun Tian[1], Ludovico Cademartiri[126*]

[1]Department of Materials Science & Engineering, Iowa State University of Science and Technology, 2220 Hoover Hall, Ames, IA, 50011
[2] Department of Chemical & Biological Engineering, Iowa State University of Science and Technology, Sweeney Hall, Ames, IA, 50011
[3]Department of Chemistry, Iowa State University of Science and Technology, 1605 Gilman Hall, Ames, IA, 50011
[4]Michigan Ion Beam Laboratory, University of Michigan, Draper Road, Ann Arbor, MI 48109, USA
[5]Instituto de Física da Universidade de São Paulo, Rua do Matão, trav. R 187, 05508-090 São Paulo, Brazil
[6] Ames Laboratory, U.S. Department of Energy, Ames, IA, 50011
[*]Author to whom correspondence should be addressed: lcademar@iastate.edu

2.1 Abstract

Removing the organic fraction from hybrid nanostructures is a crucial step in most bottom-up materials fabrication approaches. It is usually assumed that calcination is an effective solution, especially for thin films. This assumption has led to its application in thousands of papers. We here test this assumption using a relevant and highly controlled model system consisting of thin films of ligand-capped ZrO_2 nanocrystals. Consistently with carbonization, while Raman characterization fails to detect the ligands after calcination, EBS characterization demonstrates that ~20% of the original carbons are left behind even after calcination at 800C for 12hrs. By comparison plasma processing successfully removes the ligands. Our growth kinetic analysis shows that the leftover carbon can significantly affect interfacial properties.

2.2 Main Text

Organic ligands can control the growth of nanoparticles, prevent their agglomeration, and disperse them in solvents [1,2]. Nonetheless, they are often detrimental to the function of colloidal nanocrystal assemblies (CNAs), especially to those requiring good transport properties (e.g. charge transport in solid state devices [3], solar cells [4], batteries [5], fuel cells [6]) or those that require clean inorganic interfaces and surfaces in their application (e.g. catalysis [7-9]).

Several methods have been used to remove organic ligands, e.g. solvent extraction, treatment with chemical stripping agents, UV-ozone treatment, calcination, and plasma processing. Each of these approaches have drawbacks: (i) solvent extraction is generally effective on loosely adsorbed ligands and results in incomplete removal of carbon and minor grain growth [7]; (ii) chemical treatments are usually in the liquid phase (which typically disrupt colloidal assemblies due to capillary forces) and do not completely remove all ligands [9,10]; (iii) UV-ozone treatment leads to oxidation of nanoparticles and incomplete removal of carbon [9,11]; (iv) chemical oxidation by ozone leads to incomplete carbon removal (53%) and can result in oxidation [12]; (v) low temperature plasmas can effectively remove the ligands (to <1at.%) from CNAs as thick as 400nm or more [13].

Calcination at high temperatures in air remains the most common approach to remove ligands from CNAs, and, in general, to remove organics from nanostructured materials [9]. A search of the Google Scholar database yields ~60 thousand results for the keywords “template AND calcination”. While simple, this method has several limitations: (i) high temperatures can coarsen the nanoparticles [14,15] (ii) the oxidizing atmosphere can oxidize the nanoparticles (i.e.

chalcogenides, oxides of partially oxidized metals) [16], and (iii) exothermic reactions and the release of volatile byproducts can crack the CNAs [15].

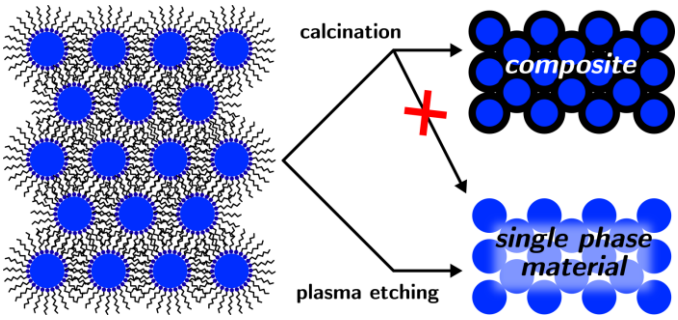

Figure 1. Schematic of the resulting microstructure after the ligand removal in colloidal nanoparticle assemblies (CNAs) by calcination and plasma processing.

In spite of these limitations, calcination is still widely used because it is equally widely assumed that it can fully remove organics from nanostructured hybrid materials in a relatively short time (recent reports claim full removal in as little as 60 seconds [8]). In the best cases the assumption it at least tested by Raman or FT-IR to show the disappearance of C-H vibrational modes [8].

In this paper, we demonstrate this assumption to be remarkably incorrect (Figure 1), at least in the case of our model system (320nm-thick film of 2.44±0.24nm ZrO_2 nanoparticles capped with trioctylphosphine oxide (TOPO), cf. Figure S1). While Raman characterization indeed shows the disappearance of the C-H modes upon calcination, EBS characterization demonstrates that as much as 17.88% of the starting carbon remains even after calcination at 800C for 12 hours. We compare these results with plasma etching on analogous samples which shows instead removal of 97% of the carbon atoms. Our findings suggest the troubling possibility that the calcination approaches ubiquitously used to convert hybrid nanostructures to

inorganic crystalline phases (e.g., block-copolymer-templated mesoporous materials, aerogels, sol-gel coatings, inverse opals) yield composites rather than the expected single-phase materials. It is especially troubling that the carbon phase left behind (most likely amorphous black carbon) is one of the hardest to detect reliably and quantitatively [17], and yet it can severely affect properties. For example, we show here that calcined CNA displays a drastically accelerated grain growth kinetics (Ea = 30kJ/mol vs 111kJ/mol) when compared to plasma processed CNAs [18].

We chose ZrO_2 nanoparticles as a model system for this study. This phase is a refractory, which opens a wide range of calcination temperatures (300^{o}C to 800^{o}C) for study. The nanoparticles are dispersed in hexane and are stabilized in the tetragonal phase (cf. Figure S1b) at room temperature due to its lower surface energy [19]. Spin coating of these hexane dispersions form films that are especially resistant to cracking [20].

The deposited CNAs were then calcined in air (300^{o}C, 400^{o}C, 500^{o}C and 800^{o}C for 1hr, 3hrs, 5hrs and 12hrs, ramp up rate of 20^{o}C $\cdot min^{-1}$ and cool down rate of 2-3^{o}C $\cdot min^{-1}$). The choice of parameters was based on the typically reported calcination conditions for nanoparticles CNAs [14-16,21]. Control CNAs were ex-posed to oxygen plasma (7W, 500mTorr, 168hrs) for compari-son [13]. Optimized conditions allow for equally effective etching in as little as 6hrs [22].

The Raman spectroscopy data from the calcined samples (Figure 2) compared to the as-deposited films, provide an initial indication of the carbon removal. The five peaks between 2840 and 3000 cm^{-1} in the unprocessed CNA correspond to the C-H saturated bond stretching in the TOPO ligand. The peaks at 2847 cm^{-1} and 2882 cm^{-1} represent the -CH_2- bond stretching modes. The peaks at 2962 cm^{-1} may correspond to the -CH_3 bond stretch. The peaks between 1100 and

1500 cm^{-1} may indicate other carbon bond stretching and are also characteristic of the ligand [23].

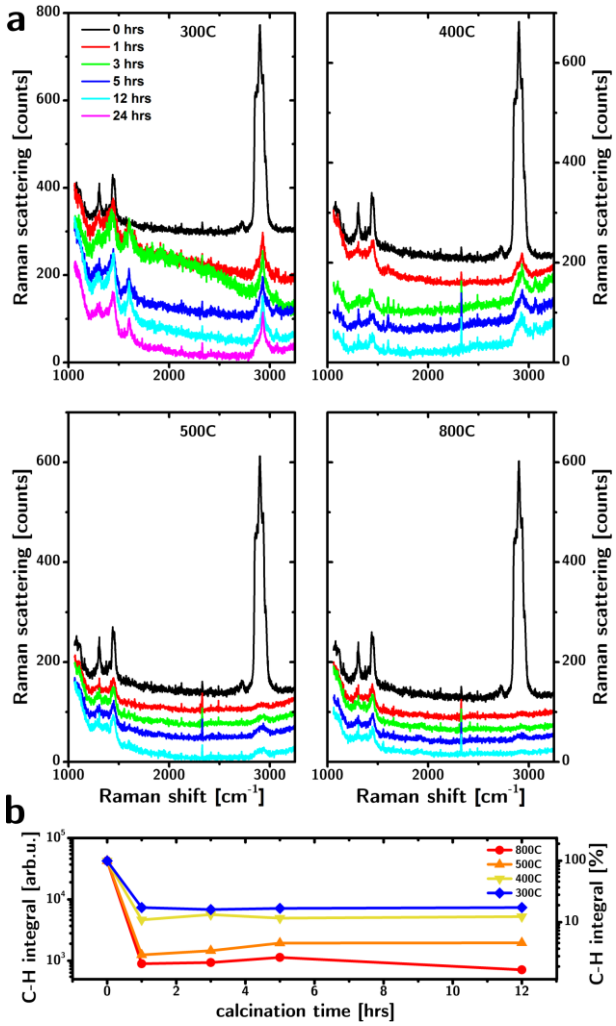

Figure 2. Effect of calcination on the C-H bond content (a) Raman spectra of the ZrO2 CNAs before and after calcination at 300ºC, 400ºC, 500ºC and 800ºC for 1, 3, 5 and 12hrs showing a reduction in the C-H content with increasing temperature. **(b)** The integral of the C-H Raman peaks for unprocessed and calcined CNAs with time, at different calcination temperatures. The plot shows a sharp decrease in the C-H content in the first 1 hour of calcination followed by a plateau, at all temperatures.

Upon calcination, the height of the peaks between 2840 and 3000 cm^{-1} decreases significantly even after 1 hour of calcination at 300ºC (Figure 2a). The height of the peaks

decreases with increasing temperature and almost vanishes at 800C. The increase in the time of calcination, results in a slow reduction in the peak heights. New peaks at 1601 and 3060 cm^{-1} appear after calcination, and are particularly prominent at 300C (Figure 2a). They might originate from decomposition intermediates which decompose or oxidize at higher temperatures.

The integral of all C-H peaks (cf. Figure 2b) shows a substantial reduction (as large as 98.3% for 800C, 12hrs) upon calcination, especially in the first 1 hour, followed by a plateau. While long calcination times do not seem to help significantly in removing the ligands, the plateau value does reduce with increasing temperatures. As the intensity of these peaks correlates with the number of $-CH_2-$ bonds, their reduction indicates the disappearance of these bonds and is in fact interpreted as a direct measure of carbon etching from thin films [8].

Since most thin films are calcined at temperatures ranging be-tween 300C-700C for times ranging between 3 and 4 hours, we compare the Elastic Backscattering Spectroscopy (EBS) spectra of a sample calcined at 400^{o}C for 5 hours and 800^{o}C at 12 hours (Figure 3a) with those of unprocessed and plasma processed films [13]. The figure clearly shows a sharp peak at 185 channel in the calcined samples, indicating significant concentrations of carbon. The area of the carbon peak is smaller for the 800^{o}C sample than for the 400^{o}C sample, which is consistent with the Raman data.

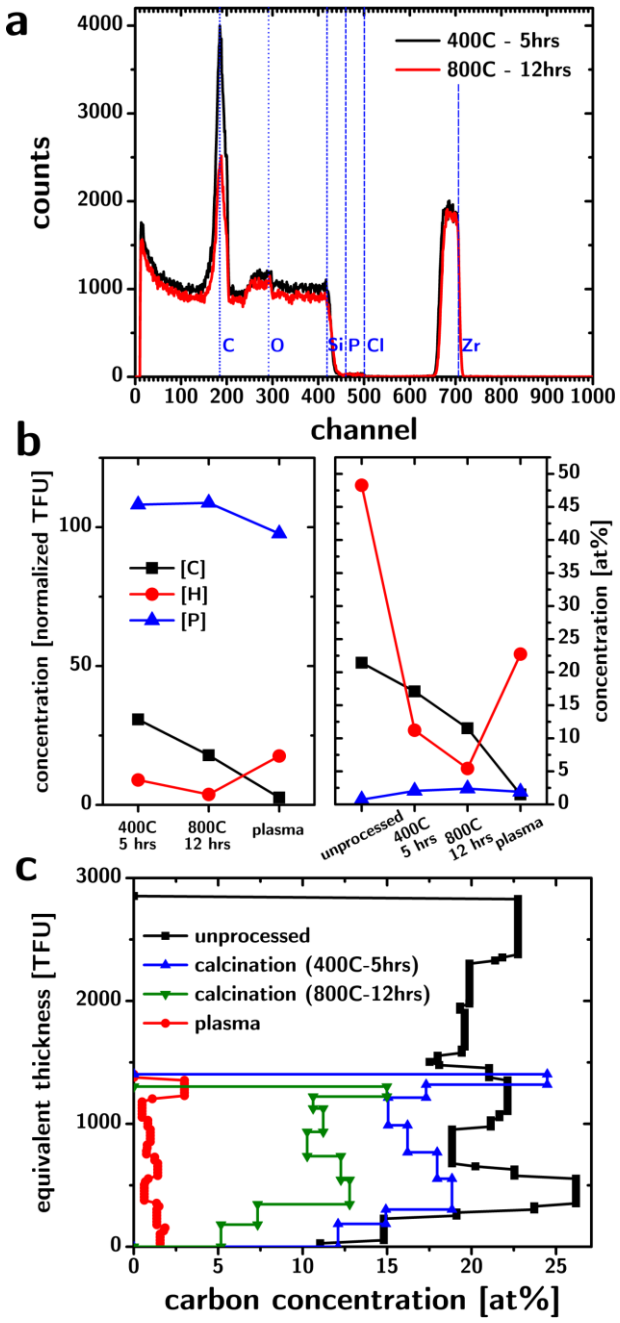

Figure 3. Chemical characterization of the CNAs after calcination and plasma processing. **(a)** Non-Rutherford elastic backscattering (EBS) spectra of the ZrO_2 CNAs after calcination at 400ºC for 5 hours and 800ºC for 12 hours, showing significant carbon content (channel 185). **(b)** (left) Concentration of C, H, and P in the films during calcination at 400ºC for 5 hours, 800ºC for 12 hours and plasma processing, normalized with respect to concentration in unprocessed CNAs. (left) and in at% (right). **(c)** Depth profile at the carbon concentration (in at%) after calcination and plasma processing.

EBS uses a high energy (MeV) ion beam to measure the number of atoms of each element per unit area (in TFU, Thin Film Units, i.e. 10^{15} atoms·cm^{-2} or at.%). For this specific measurement EBS is superior to other elemental profiling techniques like SIMS, AES, XRF, SEM (BSE) as it provides rapid, direct, accurate, and quantitative information on areal concentration of elements along with depth profiles, with a high sensitivity (<1at.% detection limit), for films as thick as 10μm [24]. Since this technique detects atoms rather than bonds (like Ra-man) or structure (like XRD), it is expected to be more reliable in the detection of overall carbon content.

Figure 3b shows the EBS-derived concentrations of C, H, and P after calcination and plasma processing. The plots represent the normalized TFU concentration of the elements with respect to unprocessed samples (left panel), and the atomic % (right panel). Calcination left behind 31% (400C, 5hrs) and 18% (800C, 12hrs) of the carbon atoms that were originally in the film. Hydrogen was instead much more severely reduced to 9% and 4% of the initial amount, respectively. Due to the effective removal of hydrogen, the concentration of carbon in the calcined samples only changes from 21at.% to 17at.% (400 ^{o}C, 5hrs) and 12at.% (800 ^{o}C, 12hrs).

The difference in the etch rates for carbon and hydrogen during calcination indicates a loss of saturation of the organic fraction (the C/H ratio in the CNAs changes from 0.44 in the unprocessed film to 2.1 in the sample calcined at 800 ^{o}C), consistent with an insufficient supply of oxygen for a fully oxidative decomposition. These carbonization conditions usually yield highly crosslinked chars and black carbon that have reduced reactivity to oxygen. Ligand removal by calcination shares similarities with the thermal decomposition of polymers, during which various processes like chain scission, cross-linking, side chain elimination, and cyclization occur [25]. The elimination of smaller molecules also leads to the formation of bonds and

crosslinking in the remaining chain. The residual crosslinked material is richer in carbon, higher in molecular weight, and is thus non-volatile. In the case of calcination, elimination of smaller hydrogenated molecules like methane, ethane, etc., through chain scission and formation of unsaturated bonds can explain the increased C:H ratio and the drastic drop in C-H peaks.

Plasma processing by comparison, reduces the number of carbon atoms by 97% (1.5 at%). A smaller fraction of hydro-gen is removed (82%), which is consistent with water adsorption. Phosphorus and zirconium (not shown) are unaffected by either treatment.

Figure 3c plots the depth profile of the carbon concentration (at.%) for unprocessed, calcined, and plasma processed films. The thickness of the CNA films is expressed in TFUs because EBS does not consider pores. Assuming a uniform density, the TFUs can be used as a measure of the CNA thickness. The plot indicates that carbon is uniformly distributed through-out the thickness of the films in all the calcination and plasma processing conditions. Our data do not support the existence of a gradient, which could be expected in diffusion-limited conditions. The higher carbon concentration at the surface of the films is due to adventitious carbon.

The diffusion of oxygen in these CNAs lies in the Knudsen regime [26] even at atmospheric pressures (Kn between 142 and 265, between 300 ^{o}C and 800 ^{o}C), due to their small pore size (~2nm). An analysis of the Knudsen diffusivity of O_2 in the pores of the CNA suggests that while the diffusivity inside the thin film is orders of magnitude lower than in air (Knudsen diffusivity between $0.8 \cdot 10^{-7}$ m^2/s at 300 ^{o}C and $1.2 \cdot 10^{-7}$ m^2/s at 800 ^{o}C, instead of a molecular diffusivity between $0.4 \cdot 10^{-5}$ m^2/s at 300 ^{o}C and $1.1 \cdot 10^{-5}$ m^2/s at 800 ^{o}C [26]), it does not limit the ligand removal due to the small thickness of the thin films. Considering an unprocessed CNAs and assuming all the carbon in it is volatile, it would take as little as 10^{-8}s for it all to diffuse out of the CNAs at room temperature. The remaining carbon after 12 hours of calcination at 800 ^{o}C

indicates that other factors limit the rate of ligand removal, like the formation of a boundary layer [27].

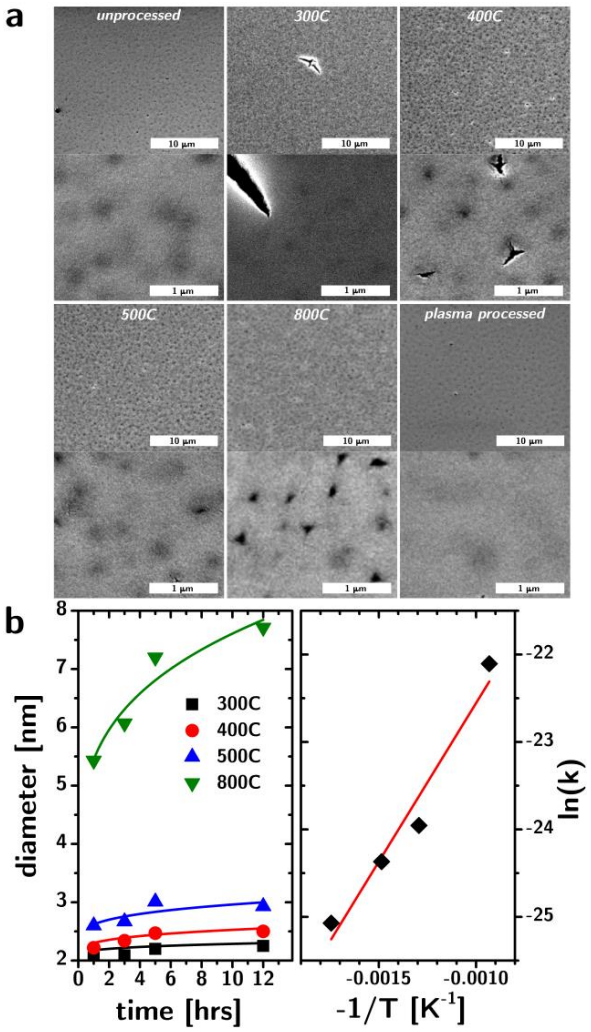

Figure 4. Surface characterization and growth kinetics of CNAs during calcination. (a) SEM micrographs of the top surface of the unprocessed, calcined (12hrs), and plasma processed films. Plasma processing produces smooth films compared to calcination, which forms deep clefts, though the disordered structure of the film resists catastrophic cracking. **(b)** Crystallite size as a function of time at different calcination temperatures with Ostwald model fit curves (left). Arrhenius plot of the rate constants of grain growth (right).

One of issues of calcination is the accompanying rapid volume loss and gas formation which can damage the structure of the material [15]. The SEM images of the calcined films show

what appear to be clefts on the surface of the films (cf. Figure 4). At higher temperatures, pits with extending microcracks can also be seen. Differently from previous reports [15], even calcination for long periods (12 hours) at temperatures (800 ^{o}C) did not cause extensive cracking in our model system. The cracks were not interconnected or intra-granular, and could therefore pre-serve some transport properties (like electrical conductivity) due to availability of a percolating path. The striking resistance to cracking in our films, compared to ordered CNAs, is consistent with the resistance to cracking upon plasma etching in disordered CNAs [20]. The plasma processed film (Figure 4) is instead smooth and crack-free.

The XRD of the calcined CNAs (cf. Figure S2) shows the diffraction peak associated with tetragonal ZrO_2 growing sharper with an increase in temperature and time, suggesting coarsening. No new phases are evident, suggesting that the remaining carbon is amorphous. Raman characterization showed no graphitization. The crystallite sizes are calculated by fitting the (111) peak and applying Scherrer analysis. At all temperatures, the crystallite sizes steeply increase in the initial time periods followed by a plateau at longer times (Figure 4b).

An Ostwald ripening model [28] is used as it describes our experimental data better than other models, [29-31] while having fewer floating parameters. The model describes the growth kinetic as $D(t)=D(t=0)+k\cdot t^{1/n}$, where t is time, $D(t)$ is the time-dependent particle size, k is the temperature-dependent rate constant and n is the growth parameter that indicates the rate limiting process in the growth kinetics [31]. The calcined samples yielded a n value of 3.6 which is significantly different from the value reported for TOPO-capped ZrO_2 nanoparticles that have been sintered only after complete ligand removal by plasma processing (2.28±0.27) [18]. This analysis suggests that the rate of diffusion of the ions at the particle/matrix boundary regulates growth kinetics in plasma processed samples, while the rate of dissolution of the surface atoms

limits growth in calcined films. The rate constants of calcined samples show an Arrhenius dependence on temperature (Figure 4c). The activation energy of grain growth of the calcined CNAs (30kJ/mol) is nearly four time smaller than the one measured in plasma processed samples (111kJ/mol) [18]. Lower activation energies suggest earlier growth/coarsening during calcination in comparison to the plasma processed samples. Since grain growth is a surface-dominated process, the significant reduction in the activation energy suggests a significant change in the interface composition resulting from the incomplete oxidation of the ligands.

2.3 Conclusion

The results shown in this work questions the widely held assumption that calcination in air is an effective method to remove organics from nanostructured precursors in order to obtain an inorganic material. Our model system consisting of thin films of ZrO_2 nanoparticles retains a significant fraction of its original carbon even after calcination at 800 ^oC for 12 hrs. A recently reported "flash" calcination approach [8] was also found to be not effective in this system. On the other hand, plasma processing appears to successfully remove the ligands from this system. Nonetheless, plasma processing still has limitations: O_2 and air plasmas can lead to oxygen implantation or surface oxidation [32], and the process takes a comparatively long time [13], even though full etching can be accomplished in 6hrs with optimized processing parameters [22].

2.4 Acknowledgement

The work described in this paper has been supported by the Member-Specific-Research-Intel program of Semiconductor Research Corporation under Award No. 2015-IN-2582. The Raman measurements were supported by the U.S. Department of Energy, Office of Basic Energy

Sciences, Division of Chemical Sciences, Geosciences, and Biosciences through the Ames Laboratory. The Ames Laboratory is operated for the U.S. Department of Energy by Iowa State University under Contract No. DE-AC02-07CH11358. XCT is grateful for a scholarship from the Chinese Scholarship Council.

2.5 Supporting Information

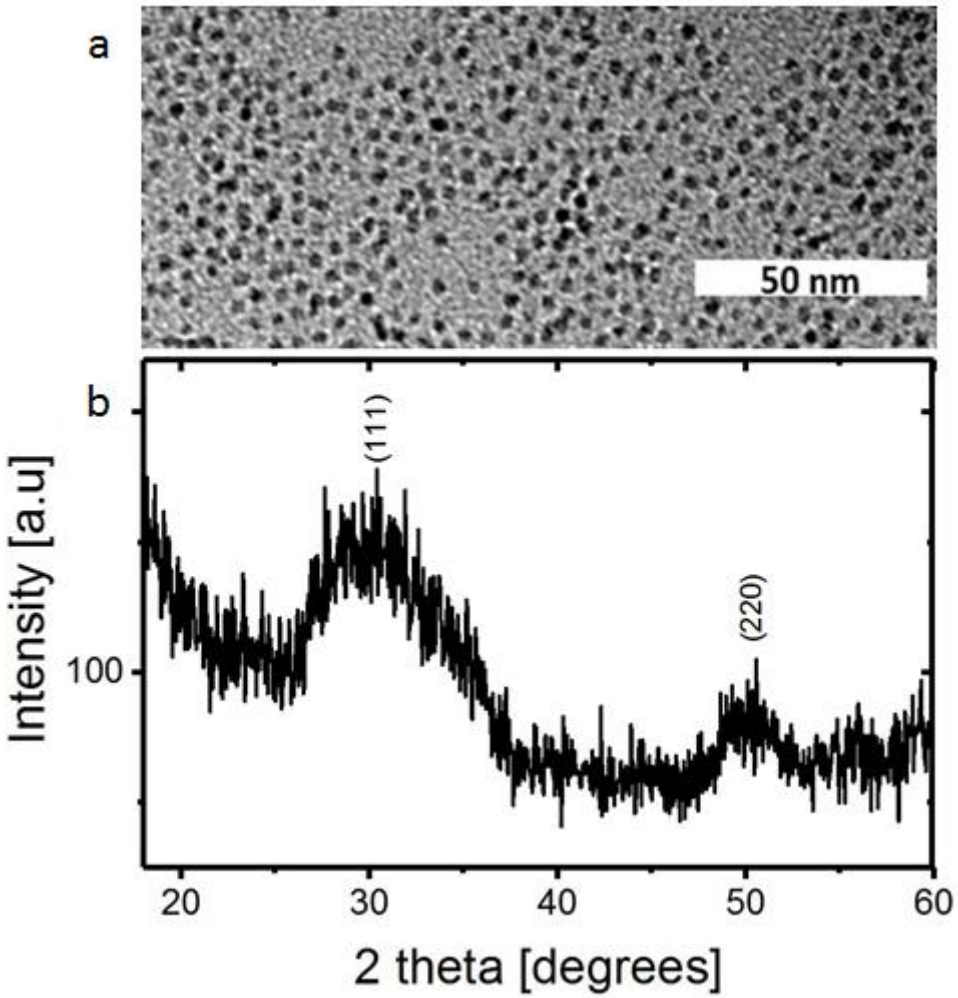

Figure S1. Morphological and phase characterization of the colloidal zirconia nanoparticles. (a) TEM micrographs of the TOPO capped zirconia nanoparticles dispersed in hexane **(b)** XRD spectrum of the unprocessed ZrO_2 nanoparticles, showing predominantly tetragonal phase.

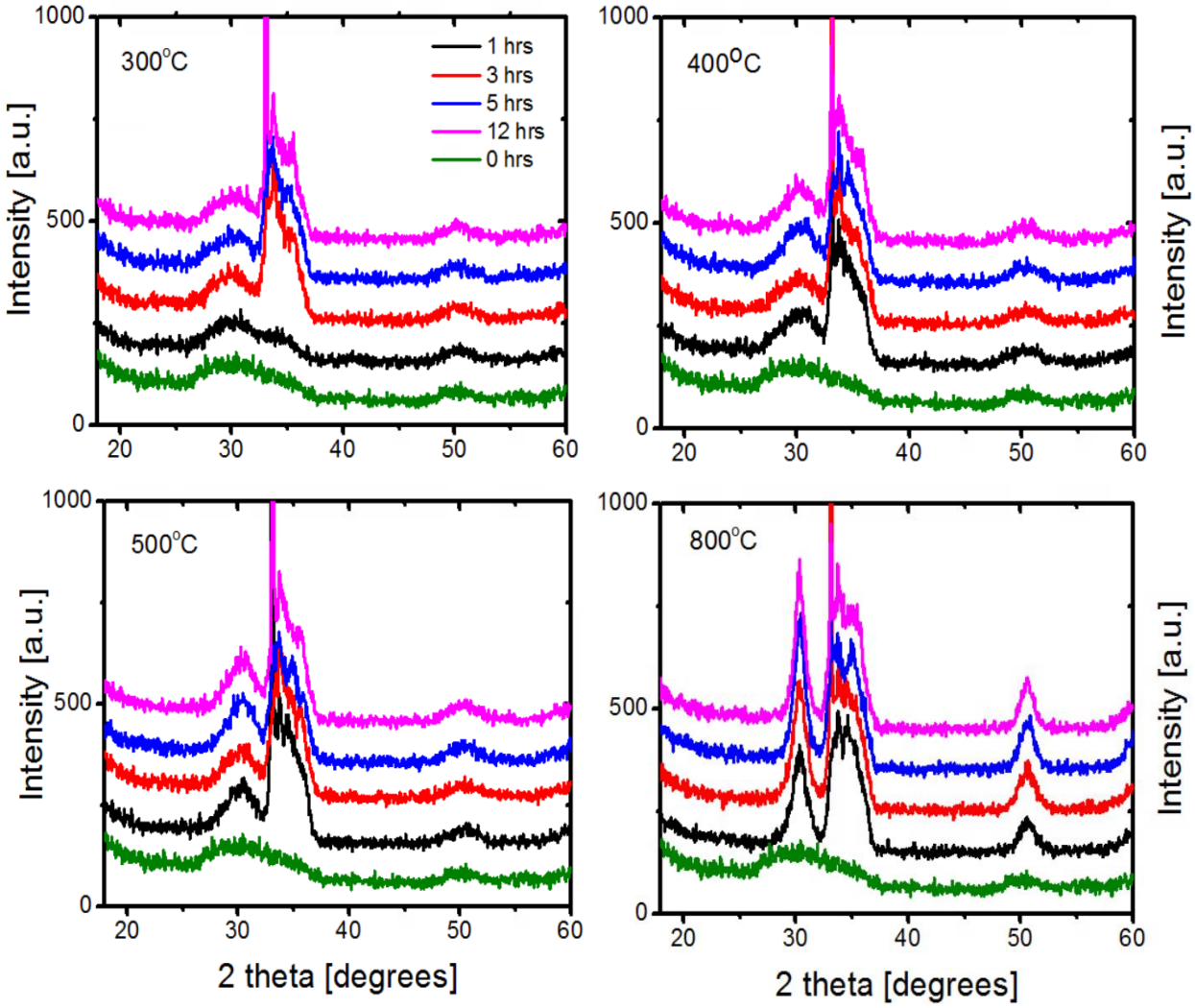

Figure S2. XRD spectra of zirconia CNAs at different calcination conditions. The plots show an increase in the tetragonal zirconia peak with the increase in temperature and time of calcination (indicating an increase in the crystallite size) and no appearance of new phases. The sharp peaks at 33-38^{o} are due to the Si substrate.

2.6 References

1. Murray, C. B.; Norris, D. J.; Bawendi, M. G. J. Am. Chem. Soc. 1993, 115, 8706-8715.
2. Cademartiri, L.; Ozin, G. A. Concepts of Nanochemistry; Wiley-VCH: Weinheim, 2009
3. Talapin, D. V.; Murray, C. B. Science 2005, 310, 86-89
4. Graetzel, M.; Janssen, R. A. J.; Mitzi, D. B.; Sargent, E. H. Nature 2012, 488, 304-312
5. Tarascon, J.-M.; Armand, M. Nature 2001, 414, 359-367
6. Scherer, G. G. Solid State Ionics 1997, 94, 249-257
7. Lopez-Sanchez, J. A.; Dimitratos, N.; Hammond, C.; Brett, G. L.; Kesavan, L.; White, S.; Miedziak, P.; Tiruvalam, R.; Jenkins, R. L.; Carley, A. F. Nat. Chem. 2011, 3, 551-556
8. Cargnello, M.; Chen, C.; Diroll, B. T.; Doan-Nguyen, V. V.; Gorte, R. J.; Murray, C. B. J. Am. Chem. Soc. 2015, 137, 6906-6911
9. Li, D.; Wang, C.; Tripkovic, D.; Sun, S.; Markovic, N. M.; Stamenkovic, V. R. ACS Catal. 2012, 2, 1358-1362
10. Gordon, T. R.; Cargnello, M.; Paik, T.; Mangolini, F.; Weber, R. T.; Fornasiero, P.; Murray, C. B. J. Am. Chem. Soc. 2012, 134, 6751-6761
11. Aliaga, C.; Park, J. Y.; Yamada, Y.; Lee, H. S.; Tsung, C. K.; Yang, P.; Somorjai, G. A. J. Phys. Chem. C 2009, 113, 6150-6155
12. Elliott III, E. W.; Glover, R. D.; Hutchison, J. E. ACS Nano, 2015, 9, 3050-3059
13. Shaw, S.; Colaux, J. L.; Hay, J. L.; Peiris, F. C.; Cademartiri, L. Adv. Mater. 2016, 28, 8900-8905
14. Babapour, A.; Akhavan, O.; Azimirad, R.; Moshfegh, A. Nanotechnology 2006, 17, 763
15. Greer, J. R.; Street, R. A. J. Appl. Phys. 2007, 101, 103529

16. Pehnt, M.; Schulz, D. L.; Curtis, C. J.; Moutinho, H. R.; Swartzlander, A.; Ginley, D. S. MRS Proceedings 1995, 382, 461

17. Lifshitz, Y. Diamond Relat. Mater. 2003, 12, 130-140

18. Shaw, S.; Silva, T. F.; Bobbitt, J.; Rodrigues, C.; Naab, F.; Yuan, B.; Tian, X. C.; Chang, J. J.; Smith, E. A.; Cademartiri, L. Chem. Mater. 2017, 29 (18), 7888–7900

19. Garvie, R. C. J. Phys. Chem. 1978, 82, 218-224

20. Shaw, S.; Yuan, B.; Tian, X.; Miller, K. J.; Cote, B. M.; Colaux, J. L.; Migliori, A.; Panthani, M. G.; Cademartiri, L. Adv. Mater. 2016, 28, 8892-8899

21. Lu, Z.; Yin, Y. Chem. Soc. Rev. 2012, 41, 6874-6887

22. Shaw, S.; Tian, X. C.; Silva, T. F.; Mohapatra, P.; Bobbitt, J.; Rodrigues, C.; Naab, F.; Smith, E. A.; Cademartiri, L. 2017, in preparation

23. Doan-Nguyen, V. V.; Carroll, P. J.; Murray, C. B. Acta Crystallogr. C 2015, 71, 239-241

24. Jeynes, C.; Colaux, J. L. Analyst 2016, 141, 5944-5985

25. Beyler, C. L.; Hirschler, M. M. SFPE handbook of fire protection engineering 2002, 2, 111-131

26. Lee, H. T. Growth, diffusion, and loss of subsurface ice on Mars: experiments and models; California Institute of Technology, 2008

27. Calvert, P.; Cima, M. J. Am. Ceram. Soc. 1990, 73, 575-579

28. Voorhees, P. W. J. Stat. Phys. 1985, 38, 231-252

29. Veshchunov, M. S. Materials 2009, 2, 1252-1287

30. Quach, D. V.; Avila-Paredes, H.; Kim, S.; Martin, M.; Munir, Z. A. Acta Mater. 2010, 58, 5022-5030

31. Huang, F.; Zhang, H. Z.; Banfield, J. F. Nano Lett. 2003, 3, 373-378

32. Cademartiri, L.; von Freymann, G.; Arsenault, A. C.; Bertolotti, J.; Wiersma, D. S.; Kitaev, V.; Ozin, G. A. Small 2005, 1, 1184-1187

CHAPTER 3. SYNTHESIS OF SILICON COLLOIDAL NANOPARTICLE ASSEMBLIES

3.1 Introduction

3.1.1 Silicon in semiconductor industry

Silicon is abundantly available on Earth, it is non-toxic and is the bedrock of the semiconductor industry. Silicon wafers cut from single crystalline silicon are used for substrates, for photochemical cells, and very widely used in the semiconductor industry for manufacturing microchips. While single crystalline silicon (sc-Si) is so incessantly used, it still has few drawbacks, that have compelled the search for other suitable options: (i) The fabrication process (that involves the Czochralski process) involves sophisticated steps, high temperatures and appreciable material loss, making the manufacturing process costly and cumbersome [1]. (ii) In photovoltaic cells, the solar conversion efficiency (solar energy to electrical energy) is limited to 18%-22% (commercial solar cells) depending on the fabrication and material quality. (iii) Single crystalline silicon has an indirect band gap (1.12eV), low visible light emission, making its application in optoelectronic devices very challenging [2]. To overcome the high manufacturing costs of the single crystalline counterpart, polycrystalline silicon was used instead, but resulted in the reduction of the conversion efficiency [3].

3.1.2 Thin films technology

Silicon thin films have an extensive applied in the microelectronic industry for making transistors, sensors, solar cells, packaging films, catalysts etc. This approach involves depositing thin layers (up to few micrometers) of semiconducting material on a substrate by processes like chemical vapor deposition (CVD), or sputtering. Different semiconducting materials like amorphous silicon (a-Si), nanocrystalline silicon (nc-Si),and other semiconductor materials: cadmium indium selenide etc. have been employed in the thin film construction.

A-Si and nc-Si have larger band gap (1.4 -2.5 eV) and higher absorption coefficient than crystalline silicon, but the manufacturing and material costs are much lower than sc-Si wafer production and it is much easier to process. A-Si has been highly utilized in semiconductor thin film technology due to its different properties but the many defects in its structure leave numerous dangling bonds that are detrimental to the band gap and need to be passivated with H bonds [4]. Even after passivation, a-Si still suffers from a high defect density. Nc-Si has instead short range crystalline order and consists of nanosize grains (10-20nm), much smaller than polycrystalline silicon, and surrounded by amorphous Si at the grain boundaries. While it is still defective, it has a larger band gap and higher absorption coefficient than sc-Si. In the nanoscale. Si displays interesting properties due to quantum confinement effects (size tunable photoluminesce [5-8]) that are not conceivable in single or polycrystalline Si, making it an interesting option for non-toxic nc light emitters.

In spite of the advantages provided by thin films, their extensive application in the semiconductor industry has been hindered by some drawbacks. (i) Thin film solar cells have low energy conversion efficiency, instability under extended exposure to light leading to degradation of its efficiency after prolonged use. (ii) The formation of the nanostructure depends very

strongly on the fabrication and processing conditions. It is difficult to control the crystallite shape and size precisely. (iii) The manufacturing process generally use CVD or sputtering, which require high vacuum conditions that are cost intensive, and use gases, like silane, SiH4, that are serious safety hazards [9].

3.1.3 Why do we need colloidal silicon nanoparticles

- Control of size of each particle: The properties of silicon are high size dependent at the nanoscale due to surface and quantum confinement effects [5]. Therefore, control of size is vital to tune the physical properties of the material. In a colloidal state, the growth of the nc-Si can be slowed down and controlled by ligand coordination.
- Control of composition: the composition and surface chemistry of the nanoparticles can be also very closely controlled by ligands and material postprocessing (e.g., plasma processing). Doping of colloidal semiconductor nanoparticles is possible [10].
- Bottom-up assembly techniques: the colloidal state of the nanoparticles allows for their processing as liquids, and their assembly in structures with highly controlled grain size, shape, and surface chemistry. With suitable processing (e.g., plasma processing), it is possible to remove all ligands from these assemblies and recover a fully inorganic nanocrystalline film with highly controlled grain size and, therefore, highly homogeneous properties down to the nanoscale.

3.1.4 Synthesis routes for silicon nanoparticles

Silicon nanoparticles are synthesized using different techniques, some of which are described below:

(i) Pulsed Laser Ablation technique: In this method, a silicon wafer is irradiated with a laser pulse (10-15 sec- 10-9 sec), under an inert gas. The gas pressure conditions [11] irradiation parameters like laser energy, repetition rate, pulse rate [12] affect the size of the nanoparticles. A range of nanoparticle size can be synthesized (5nm – 65nm [13]) that can be further controlled by post processing etching processes.

(ii) Attrition ball milling: In this method, silicon dioxide and carbon (graphite) are ball-milled for few days (7-10 [14]), followed by an annealing step at 150^{o}C, to synthesize silicon nanoparticles with sizes around 5nm. The drawback of this synthesis technique is that it produces nanoparticle sizes varying in a wide range and has agglomeration issues leading to a non-uniformity in the particles generated.

(iii) Physiochemical methods: Silane precursors dissociated by heating with CO_2 laser along with SF_6 and H_2 to give silicon powders. The size of the nanoparticles produced is generally small (5-10nm [15]). The nanoparticles can be then deposited on a substrate on transferred to a liquid medium for further processing. The size of the particles is generally well controlled.

(iv) Chemical methods: Silicon hydrides are reduced by agents like lithium aluminum hydride [16], zyntyl compounds in suitable surfactants/solvents (like alkyl tricholosilane) to produce silicon nanoparticles that are hydride ended and can be capped with ligands. The nanoparticles produced are monodisperse and can be synthesized for a wide range of sizes.

(v) Thermal decomposition: Thermal degradation of silicon rich precursors like hydrogen silsequinone [17] in reducing atmospheres to yield a matrix of silicon nanoparticles in a silica matrix. The matrix is then etched by HF etchant to produce hydride ended silicon nanoparticles that can be directly dispersed or are capped with ligands to disperse in solvents. Size tunable photoluminescent nanoparticles are synthesized.

3.1.5 Problems associated with the synthesis of colloidal silicon nanoparticles

- Precursors: the precursors used are generally costly, and highly reactive for the thermal treatment synthesis of silicon nanoparticles.
- Yield: The yield of Si nps from such precursors are low (less than 10% mass yield [5])
- Synthesis temperature: the temperatures used for heat treatment are high (above 1100oC) [18], thus requiring high temperature furnaces with controlled atmospheres (high energy and material consumption).
- Safety: Highly concentrated hydrofluoric acid (highly toxic and corrosive) is generally used in the etching of the matrix [5,19], which requires special safety precautions for handling and storage.
- Cleaning: the synthesis procedure often fails to remove all unreacted precursors and fails to completely remove the matrix leaving behind materials that are partially oxidized, having high concentrations of organics, and therefore difficult to characterize and study.

3.1.6 Objective of this work

Here in this section, we work on the low-cost synthesis of crystalline Si nanoparticles with control of size below 5nm, high purity and their deposition as CNAs, plasma processing to remove the ligands, and their RIE etching for patterning.

3.2 Results and Discussion

Figure 1a shows a schematic of the synthesis of silicon nanoparticles. The silicon nanoparticles were synthesized based on the method described previously by G.A. Ozin et. al. [5]. Commercial silicon monoxide SiO powders (-325 mesh, from Sigma Aldrich) were used as the starting material, as they have a higher silicon content, are cheap and readily available in bulk. The SiO powders were placed in an alumina boat and placed in a tube furnace which was then flushed with 95% H_2 and 5% Ar for 1 hour, to remove any oxygen present inside the tube furnace. Under a continuous flow of the shielding gas, the samples were heated to the designated temperatures (900^{o}C,1000^{o}C and, 1100^{o}C), held for decided time periods (1,2,3,5 and 10 hours) and the cooled down to room temperature.

a

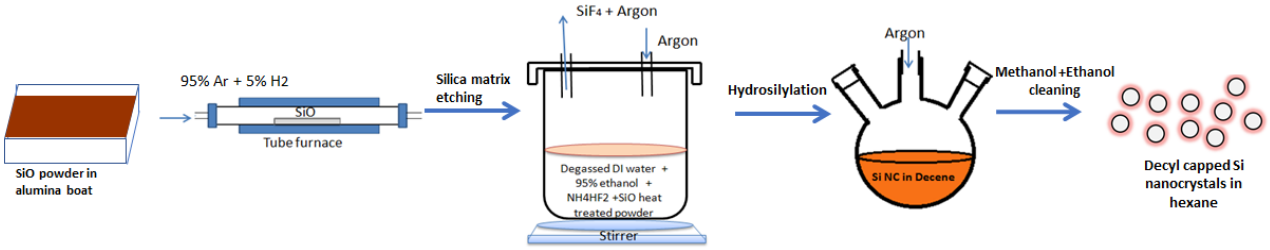

b

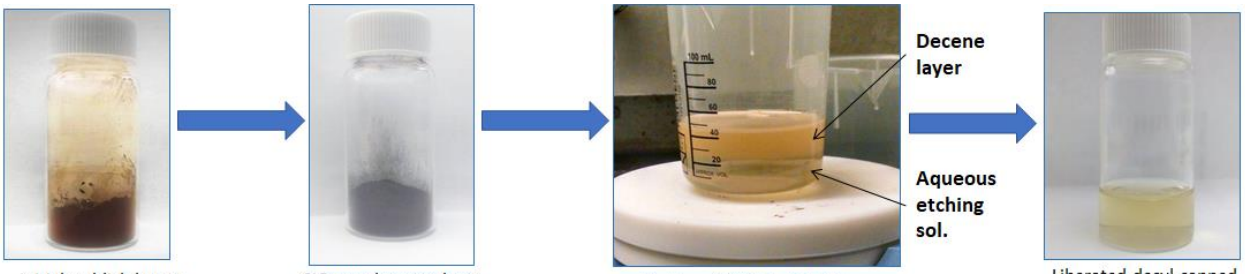

Figure 1. (a) Schematic representation of the synthesis process of the colloidal silicon nanoparticles from SiO powder (b) From SiO powders to liberated decyl capped dispersed Si ncs in hexane

Silicon monoxide is a unique oxide of silicon because of the unusual valence state of silicon (+2). Though this structure has been argued to be a mixture of pure amorphous silicon and silicon dioxide, Hirata et al. [20] show that amorphous silicon monoxide consists of regions of amorphous silicon and silica with suboxide (SiO_x) type tetrahedral structure in the interface which acts as a transition bridge between the random amorphous structure of silicon and silicon dioxide. Studies on annealing amorphous silicon monoxide showed structuring of these regions into definite silicon and silicon dioxide regions[21]. On heat treating silicon monoxide, these clusters of amorphous silicon can be considered to act as the sites of initiation of nucleation of crystalline silicon nanoparticles. The heat treatment of commercially available amorphous silicon monoxide powders (broad peaks in the XRD spectrum centered around 23 and 51 degrees [5, 22]) in a reducing atmosphere results in the thermal disproportionation of silicon monoxide into silicon and silicon dioxide. The size of the synthesized nanoparticles ranges from 2.2-5.3nm, depending on the process parameters used. The reddish-brown silicon dioxide becomes dark blackish brown after heat treatment as seen in fig 1b. This blackish brown powder now consists of silicon nanoparticles surrounded in a matrix of silicon dioxide.

The heat treatment has three key controllable parameters: temperature, time, and atmosphere. After heat treatment of SiO at 900^{o}C (shown to be the optimum temperature of silicon crystallization nucleation by G.A. Ozin et. al [5]) for 35 mins, a small peak appears at 28° on the broad peak at ~23° (attributed to SiO_2) and two peaks at 47° and 55° corresponding to (111), (220), and (311) planes of silicon. As the temperature of processing and holding time are increased, the peak at 28° grows in intensity and sharpness and the height of the broad peaks at 23° and 51° diminish: the temperature and holding time of heat treatment of the SiO powders

control the size of the silicon nanocrystals. Fig 2a shows the XRD patterns of the SiO powders heat treated at temperatures of 900°C and 1000°C for increasing time periods ranging from 1 to 10 hours. The size of the Silicon nanocrystal is calculated using the Scherrer equation on the peak at 55°. At a constant temperature of 1000°C, particle size increases almost linearly with time in the initial holding times and then reaches saturation (cf. Fig 2b). The effect of heat treatment parameters on the crystallite size was also studied with TEM analysis (cf. Fig 2c-2g). The images show distinct lattice planes and thus prove that the nanoparticles are crystalline and do not lose their crystallinity during the processing. The images also confirm the increase in the average size with temperature and holding time. No amorphous region can be seen at the surface of the particles.

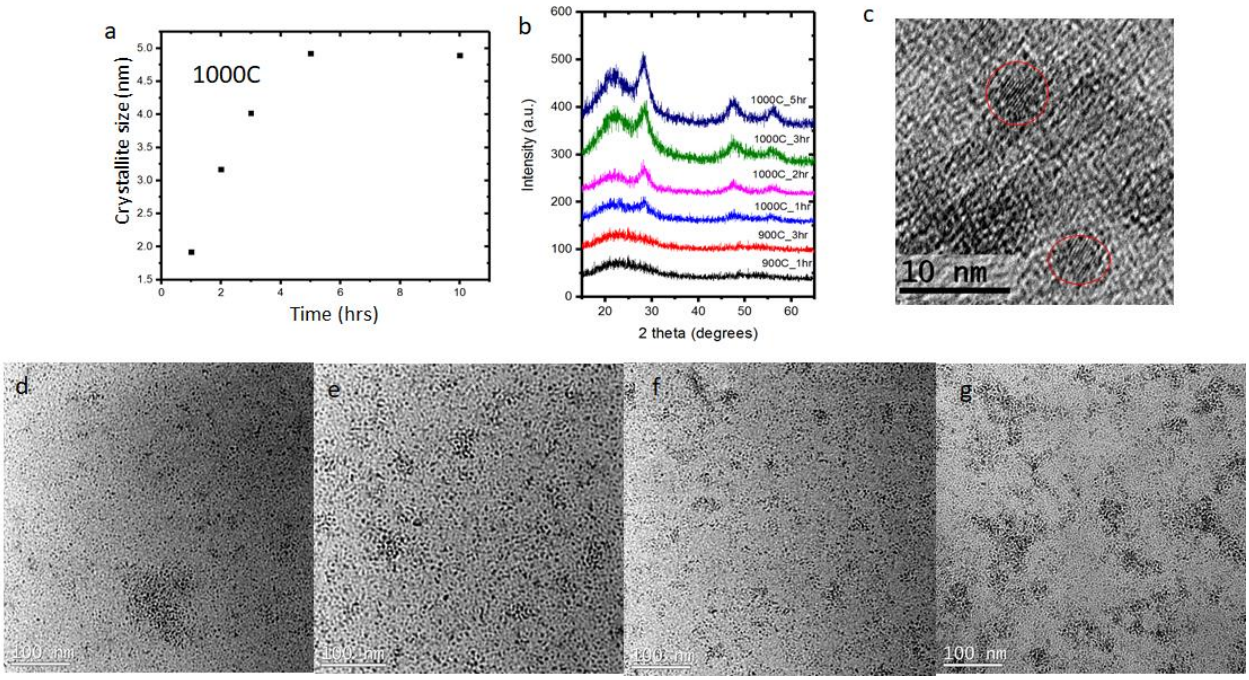

Figure 2. (a) Particle size change with time of holding at 1000°C heat treatment temperature. (b) XRD patterns of the heat treated SiO powders ar different temperature and times. (c) TEM of liberated decyl capped Si nanoparticles showing lattice fringes. TEM micrographs of Si ncs after (d) heat treatment :1000°C_2hr, Particle size : 3.6 + 0.9 nm (e) heat treatment :1000°C_3hr, Particle size : 3.7 + 0.8 nm (f) heat treatment :1000°C_5hr, Particle size : 4.3 + 0.8 nm (g) heat treatment :1100°C_10hr, Particle size : 5.3 + 1 nm

The atmosphere of 5% H_2 and 95% Ar has been shown to provide the optimum protection against oxidation and to enhance the crystallinity during heat treatment [23,24]. Experiments conducted with 5% H_2 and 95% N_2 in the same temperature and time conditions provided lower crystallinity than 5% H_2 and 95% Ar. This can be attributed to better O_2 displacement by Ar as compared to N_2.

In order to liberate the silicon nanoparticles, the silica matrix has to be selectively removed without damaging the silicon nanocrystals. The typical approach is to use an HF etching to liberate hydrogenated ncSi (hydrogen terminated silicon nanoparticles). [5,25] The etching mixture typically consists of 95%ethanol and 48% hydrofluoric acid in a 1:2 ratio. To reduce the risk profile and have a slower and more controllable etch, we substituted 48% HF with 6 mol% ammonium bifluoride (NH_4HF_2) in deionized (DI) water. The heat treated SiO powders are transferred to a plastic beaker and stirred continuously for 6 hours in the etchant solution (6 mol% NH_4HF_2 in DI water + 95%ethanol in 1:2 ratio).

Ammonium bifluoride is a white crystalline solid that has no reported amount of HF in its solid phase, which makes its storage and handling much safer than 48% HF. In water, ammonium bifluoride dissociates to form NH_4F, H+ and F-. Thus, HF is generated in situ, where it can immediately react with the SiO_2 according to the reaction:

$$SiO_2 + 4NH_4HF_2 \rightarrow 4NH_4F + 2H_2O + SiF_4$$

where NH_4F and H_2O remain in solution and SiF_4 leaves the system as a gas. While ammonium bifluoride is safer to handle, the etching time periods are longer as compared to HF etching. The studies on optimizing the time and concentration of etchant have not been included in this study. The evolution and exit of SiF_4 helps in driving the etching reaction forward. Therefore, the atmosphere of the reaction also plays an important role during etching. Etching

carried out in ambient atmosphere led to drastically reduced yields, with evidence of unetched matrix at shorter etch times and almost no product at longer etch times (20 hours). Fig 3a-b shows the dispersion of the liberated silicon nanoparticle in hexane after short and long etch times. The characteristic orange color of the dispersion is present in the short etching durations but fades almost completely after 20 hours. The TEM micrographs of the corresponding solutions are shown in fig 3c-d. For short etch times, the liberated and hydrosilylated silicon dispersion show dense fuzzy mass around the nanoparticles. For longer etching times, the fuzzy mass is not present, but wire like structures surrounding the silicon nanoparticles can be seen. On etching for even longer times, no particles or fuzzy masses are obtained. Such fuzziness and wire like structures can be explained as unetched portions of silica matrix surrounding the nanoparticles.

As the etching of the silica matrix proceeds, the silicon nanoparticles are liberated in the solution where they are highly susceptible to oxidation owing to exposure and their large surface area. Any oxygen available can cause oxidation to silicon dioxide, which can then be converted to SiF_4 by the etchant and leave the system, therefore leading to drastic yield loss. Oxygen can originate from two sources: O_2 dissolved in the DI water, and dissolution of atmospheric O_2 in the solution during stirring. The dissolved O_2 was removed by degassing the DI water prior to forming the etching solution. To prevent dissolution from atmosphere, the etching set up was flushed with Ar throughout the etching time (cf. Fig 3e), which maintained an inert atmosphere above the etching solution and displaced the lighter SiF_4 product out from the system. Fig 3f-g shows the TEM micrographs of the silicon liberated after 3 and 6 hours of etching in degassed DI water and Ar atmosphere. While some evidence of unetched matrix can still be seen after 3 hrs, after 6 hrs fully liberated and matrix free silicon nanoparticles are seen in Fig 3g.

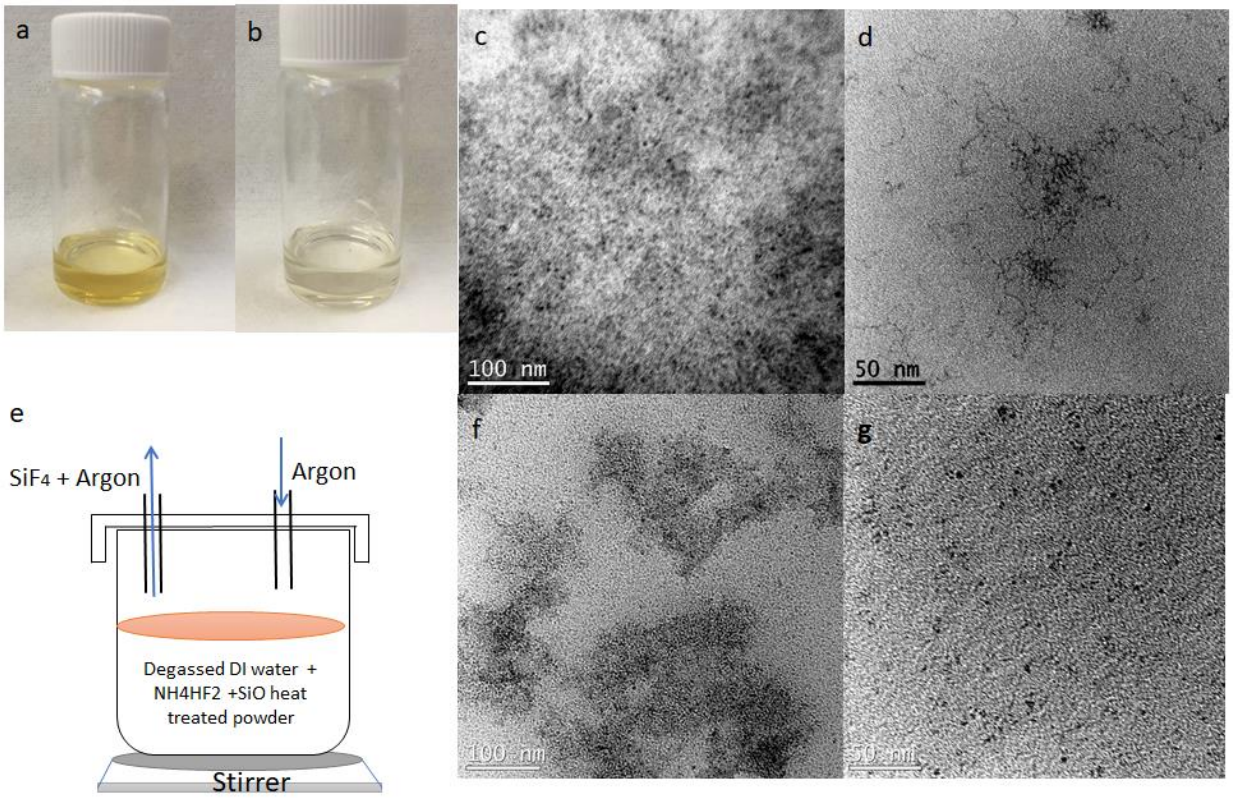

Figure 3. (a) Dispersion of silicon nanoparticles in hexane after etching for 3.5 hours (b) 20 hours (c) TEM of dispersion of silicon nanoparticles after etching for 3.5 hours (d) 20 hours (e) schematic of Ar flushing during etching reaction (f) TEM of dispersion of silicon nanoparticles etched in Ar flushing after 3 hrs (g) 6hrs

The silicon nanoparticles liberated from the silica matrix are hydride terminated (ncSi:H) and have limited colloidal stability in organic solvents, which can be drastically improved by capping with organic ligands through hydrosilylation. Silicon is highly sensitive to oxygen and the organic decyl ligand cap also prevents the rapid oxidation of the silicon nanoparticles to silicon dioxide. A terminal olefin – 1-decene – is used to extract the ncSi:H from the aqueous etching solution. 100ml of 1-decene was added to 200ml of etching volume after the etching time and stirred for 5 mins under inert atmosphere. A transfer of the ncSi:H nanoparticles from the

etchant solution to top decene was observed as a transfer of the orange color associated with the Si ncs. After the transfer, the top decene layer carefully collected into a 3-neck round bottom flask. Care was taken not to include any aqueous etchant solution during the separation. The organic phase was then heated at 170^{o}C for 20 hours to generate decyl-capped nanocrystalline silicon [26], which are then dispersible in non-polar organic solvents like hexane and toluene.

3.2.1 Formation of thin films by spin coating

The dispersion of colloidally stable Si nanocrystals in organic solvents can be processed to form colloidal nanocrystalline assemblies (CNAs), from which the ligand can then be removed by plasma processing (cf. Figure 4). Spin coating of the hexane dispersions onto a silicon substrate yields a uniform thin film. The thickness of the thin film CNA can be varied by changing the concentration of the dispersion or by modifying the spin casting conditions. As shown by Shaw et al, CNAs deposited from hexane are disordered and crack-free and remain crack-free during ligand etching by plasma and further sintering [27]. The findings apply also in this case, as shown in Figure 4b and 4c. Fig 4b shows the SEM micrographs of the as deposited thin films. CNAs ranging in thickness between 160nm and 570nm were obtained by changing the concentration of the dispersion.

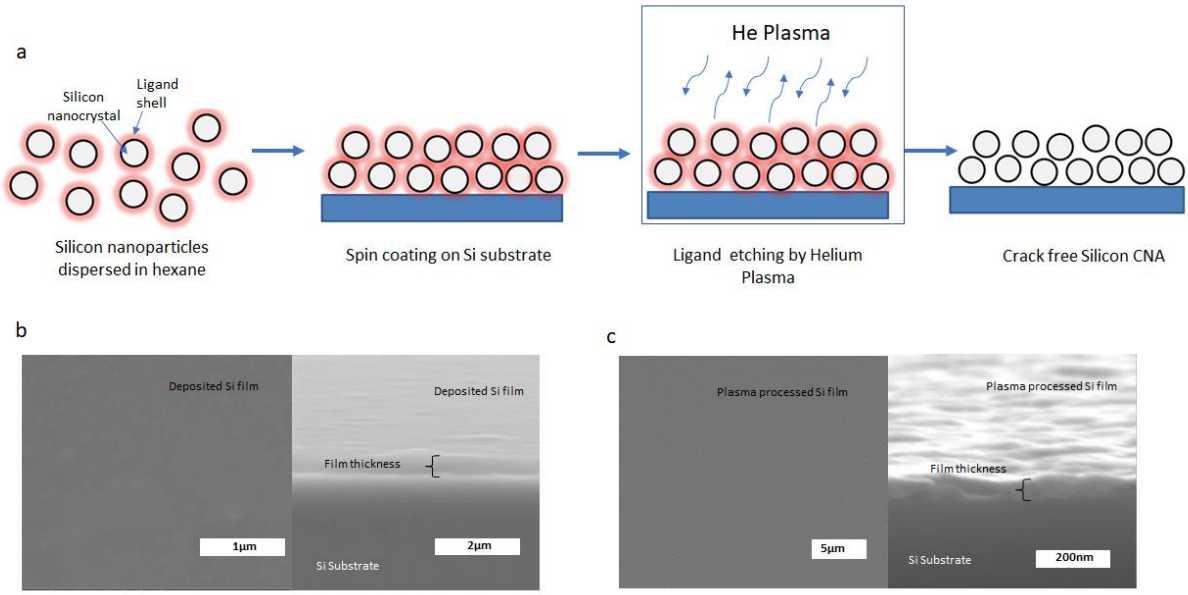

Figure 4. (a) Schematic of thin film deposition by spin coating and ligand removal by plasma processing. (b) top and side of the as deposited thin films (c) after plasma processing

3.2.2 Plasma treatment of spincoated Si nc thin films

While calcination might appear to be a simple solution to the problem of removing the organic ligands from the Si CNAs, our work described in the previous chapter demonstrates that it only leads to composites with starkly different physical properties. Silicon, differently from oxides presents further challenges as a candidate for calcination. Silicon, being a metal, is more prone to grain growth on calcination than metal oxides even at lower temperatures, and is very sensitive to oxidation. Annealing of silicon has been done in different methods like rapid thermal annealing [28], or flash lamp annealing [29]. These methods lead to sintering and coarsening and do not generally remove the entirety of the ligands (as demonstrated in previous chapter).

The removal of the organic decyl ligands is carried out by exposing the deposited silicon films to low temperature plasma. Helium plasma and 5%H_2/95% Helium plasmas were used as the feed gases to avoid the oxidation associated with the more commonly used O_2. Other inert plasma feed gases are Ar and N_2, but these gases were not employed to avoid nitrogen implantation [30] and sputtering of the silicon atoms by the heavy N and Ar ions [31]. The deposited thin films were exposed to room temperature plasma at 500 mTorr, 30W He plasma for 24 hours. The reduction in the thickness is due to the removal of carbon and loss of solvent from the films. The thickness of the plasma treated thin films ranged from 220 to 35 nm. Fig 4c shows the top and cross section of the plasma treated silicon thin films: even after ligand removal and the associated large volume loss, the surface of the films is crack free, which is consistent with the findings of our laboratory for disordered CNAs thinner than 450nm [27].

Raman spectroscopy of the unprocessed and plasma processed (24hr, 95%He/5% H2) thin films is shown in Fig 5a. The four peaks from 2850-2990 cm-1, present in the unprocessed sample correspond to the C-H bond stretching and are expected to arise from the decyl ligands. The intensity correlates with the number of C-H bonds present. The peak at 1290 cm-1 corresponds to the Si-CH3 stretch in silanes and suggests the hydrosilylation of the nanoparticles by decene. Plasma processing causes all of these peaks to disappear, suggesting a removal of the C-H and Si-CH bonds in the plasma processed films.

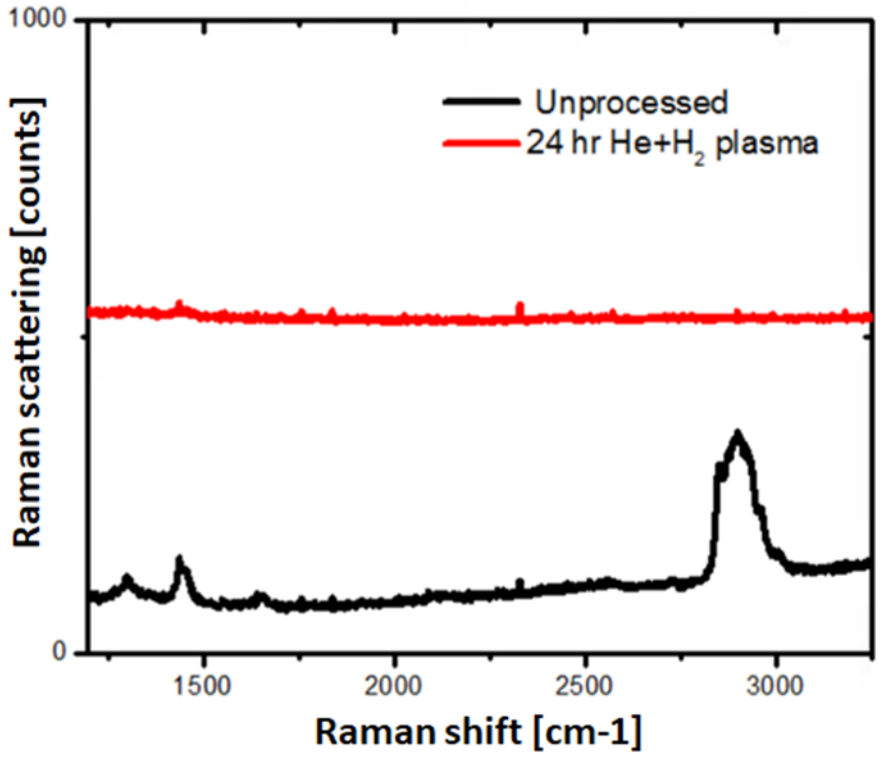

Figure 5. Raman spectroscopy of unprocessed and 24hr 95%He + 5%H_2 plasma processed Si nanoparticle thin films

3.2.3 Effect of sample processing on film quality

The quality of the thin films was observed to depend on some aspects of the nanoparticle processing:

Effect of excess ligand: The hydrosilation of silicon nanoparticles is carried out in decene and insufficient cleaning of the nanoparticles may result in the inclusion of excess decene in the hexane dispersion in hexane. This excess organic lead to the formation of ridges and undulations on the film surface upon spin-coating, especially at the edges where the film is thickest (Fig 6 a). These contours persist after plasma treatment. Excess ligands also increase the plasma etching

time required for complete carbon removal. Radial striations were also observed in spin coated sol-gels and are expected to depend on volatility, viscosity and surface tension properties of the solvent [32]. Thoroughly cleaning the dispersions by repeated precipitation, centrifugation and redispersion resolves the issue: Fig 6b shows the smooth top surface of the film formed after 3 cleaning cycles.

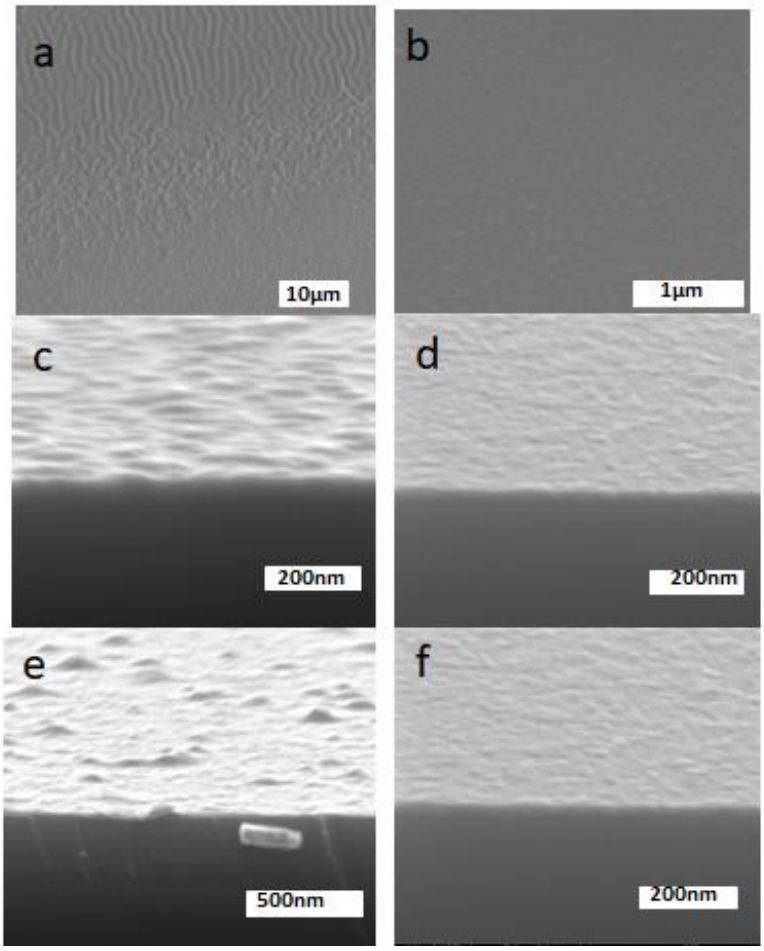

Figure 6. (a)Top surface of films containing excess decene with undulations/striations (b) the top surface of the film formed after 3 cleaning repetitions (c) Top surface of thin films with clusters of inhomogeneities present even after the plasma treatment (d) smooth surface of film after complete etching of the SiO_2 matrix (e) clusters on film surface formed after etching of silica matrix in non inert atmosphere (f) smoother films after etching of silica matrix in inert atmospheres

Effect of incomplete etching of SiO_2 matrix: The complete etching of silica matrix in the aqueous NH_4HF_2+ethanol is essential for the liberation of the silicon nanoparticles. If the etching of silica matrix is incomplete due to shorter etching times, it is then difficult to remove it during the subsequent hydrosilylation and cleaning steps (cf. Fig 3f). The films prepared from these dispersions (Fig 6c) shows clusters of inhomogeneities on the film surface before and after the plasma treatment. The issue is resolved upon complete etching of the films (Fig 6d).

Effect of O_2 traces and shorter etching times: Using non-inert etching atmospheres results in simultaneous etching of the matrix and the silicon nanoparticles, as discussed earlier. As a result, the silicon nanoparticles are never completely liberated from their silica matrix (cf. Fig 3c, d). The presence of the silica matrix also affects the thin film morphology as discussed above and produces inhomogeneities/clusters on the film surface (cf. Fig 6e). Using an inert atmosphere and adequate etching times results in smoother films (cf. Fig 6f).

3.2.4 Reactive ion etching

Given the expected porosity of our ligand-free nc-Si CNA, it was important to compare the rates of reactive ion etching of these materials to established standards (e.g., a-Si, sc-Si). Silicon thin films have an extensive use in the semiconductor industry where they undergo different steps of etching and doping to finally create a transistor or other devices.

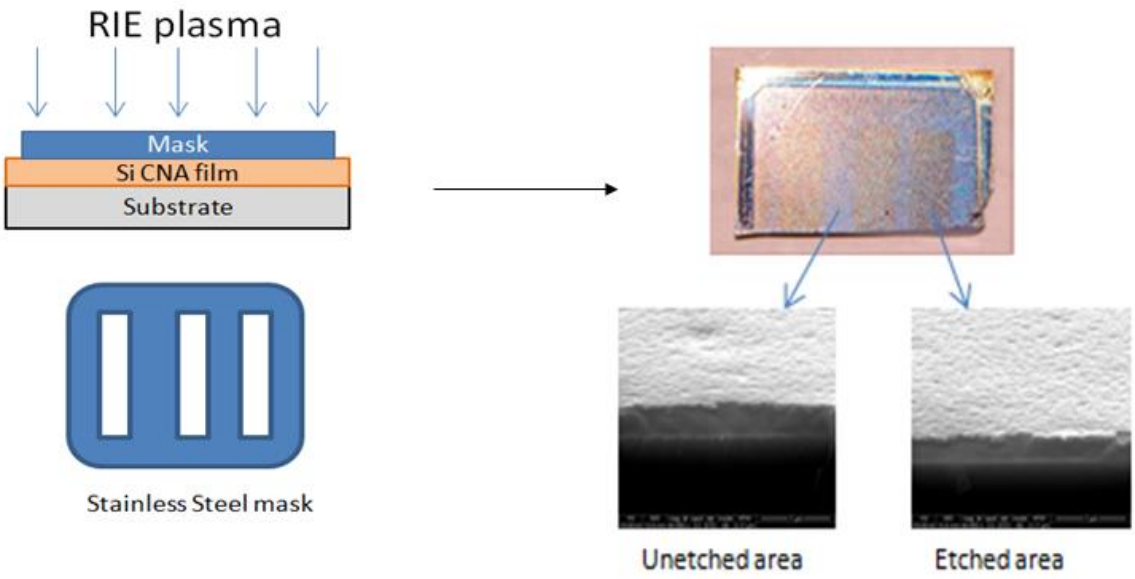

Figure 7. Schematic representation of Reactive Ion Plasma Etching experiment

A schematic of the Reactive Ion etching process is shown in Figure 7. The thin films were exposed to SiF_6 plasma conditions that were calibrated to yield a 0.45nm/sec etch rate on sc-Si. An aluminum mask with open slots (cf. Fig 7) was placed on top of the ligand-free CNAs during RIE, after which the thicknesses of the exposed and unexposed areas were compared to obtain an estimate of the etch rate. Figure 8 shows the SEM micrographs of the etched and unetched areas of the 5.3nm silicon nc thin films after RIE. The thickness reduced from 419±20nm to 328±23nm in 90sec giving an etch rate of 1.01±0.47 nm/sec. A repeatability study on the etching rates on films with the same nanoparticle sizes (5.3nm) found an etch rate of 1.17± 0.6 nm/sec. The rate of the RIE of the CNAs was found to be 2.2 – 2.5 times larger than the etch rates of single crystalline silicon.

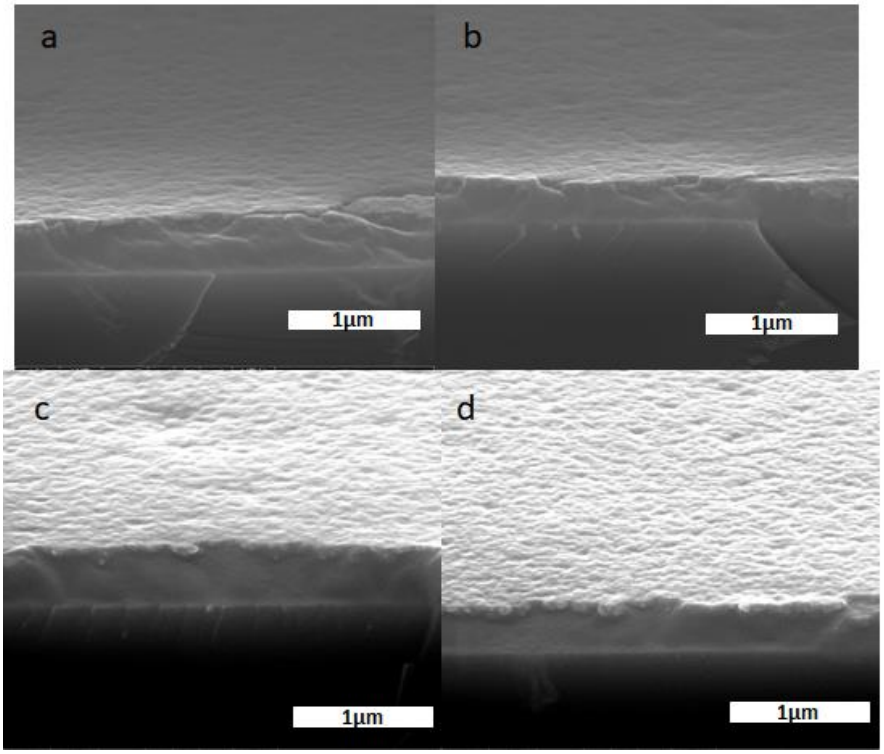

Figure 8. RIE etching of plasma processed Si np(5.3 nm) thin films in SF_6/O_2 (a,c) masked unetched area (b,d) etched area

The scatter in the data originates from a number of factors: (i) the imperfect flatness of the spin-coated film, (ii) the potential inhomogeneity in the content of residual carbon, (iii) the high etch rate of SF_6, (iv) the small thickness of the films, and (v) the resulting short times of exposure. The higher etch rate in the nanoparticle thin films can be attributed to the porosity in the films formed after the removal of ligands. The pores would allow a higher penetration of the non-ionic etchant species as compared to single crystalline silicon resulting in faster etching rates.

3.3 Conclusion

The work in this chapter demonstrates a low cost, safer to handle, technique to fabricate silicon nanoparticle thin films from colloidal silicon nanoparticles and removal of ligands using non-oxidizing plasma. Raman spectra show a complete removal of carbon in the films. The process parameters affect the size of nanoparticles and the quality of the thin films produced. The plasma processed, crack free thin films are seen to have almost 2 times faster reactive ion etch rates than commercial standard single crystalline silicon, which may be attributed to higher porosity of the CNA thin films. The size of the nanoparticles is also expected to affect the etch rates.

3.4 References

1. Haynes, W.M. CRC Handbook of chemistry and physics, 93rd edition. Taylor Francis, Bacon Raton 2012

2. Nesheva, D.; Raptis, C.; Perakis, A. Journal of Applied Physics 2002, 92, 4678

3. Hermann A. M. Sol E Mater Sol cells 1998, 55, 75–81

4. Staebler, D. L.; Wronski, C. R. Applied Physics Letters, 1977, 31, 292-294

5. Sun, W.; Qian, C.; Cui, X. S.; Wang, L.; Wei, M.; Casillas, G.; Helmy, A. S.; Ozin, G. A. Nanoscale, 2016, 8, 3678

6. Mastronardi, M. L.; Henderson, E. J.; Puzzo, D. P.; Ozin, G. A. Adv. Mater. 2012, 24, 5890-5898

7. Hessel, C. M.; Reid, D.; Panthani, M. G.; Rasch, M. R.; Goodfellow, B. W.; Wei, J.; Fujii, H.; Akhavan, V.; Korgel, B. A. Chem. Mater. 2012, 24, 393-401

8. Wilson, W. L.; Szajowski, P. F.; Brus, L. E. Science 1993, 262, 1242-1244

9. Bloem J.J, Claassen W.A.P. J Cryst Growth 1980 49, 3

10. Norris, D. J.; Efros, A. L.; Erwin, S. C.; Science 2008, 319

11. Yoshida, T'; Takeyama, S.; Yamada, Y.; Mutoh, K. Appl. Phys. Lett. 1996, 68, 1772

12. Wang, Y. L.; Xu, W.; Zhou, Y.; Chu L. Z; Fu, G. S. Laser and Particle Beams 2007, 25 ,9

13. Intartaglia, R.; Bagga, K.; Scotto, M.; Diaspro, A.; Brandi, F. Opt. Mater. Express 2012, 2, 510

14. Lam, C.; Zhang, Y. F.; Tang, Y. H.; Lee, C. S.; Bello, I.; Lee, S. T. J. Cryst. Growth 2000, 220 466

15. Erogbogbo, F.; Yong, K. T.; Hu, R.; Law. W. C.; Ding, H.; Chang, C. W.; Prasad P. N.; Swihart, M. T. ACS Nano 2010, 4, 5131

16. Sudeep, P. K.; Page, Z.; Emrick, T. Chem. Commun 2008, 46 6126

17. Hessel, C. M.; Reid, D. K.; Panthani, M. G.; Rasch, M. R.; Goodfellow, B. W.; Wei, J.; Fuji, H.; Korgel, B.A. Chem. Mater., 2012, 24, 393–401

18. Hessel, C. M.; Henderson, E. J.; Veinot, J. G. C. Chem. Mater., 2006, 18, 6139–6146

19. Yu, Y.; Rowland,C. E.; Schaller, R. D.; Korgel, B. A. Langmuir 2015, 31, 6886-6893

20. Hirata,A.; Kohara, S.; Asada, T.; Arao, M.; Yogi, C.; Imai, H.; Tan, Y.; Fujita, T.; & Chen, M.; Nature Communications 2016, 7,11591

21. Hohl, A.; Wieder, T.; van Aken, P. A.; Weirich, T. E.; Denninger, G.; Vidal, M.; Oswald, S.; Deneke, C.; Mayer, J.; Fuess, H. J. Non-Cryst. Solids, 2003, 320, 255–280

22. Sun, W. Qian, C. Wang, L. Wei, M. Mastronardi, M. L. Casillas, G. Breu J. and Ozin, G. A. Adv. Mater., 2015, 27, 746–749

23. Li, Y.; Liang, P.; Hu, Z.; Guo, S.; You, Q.; Sun, J.; Xu, N.; Wu, J. Appl. Surf. Sci. 2014, 300, 178–183

24. Borrero-González, L. J.; Nunes, L. A. O.; Andreeta, M. R. B.; Wojcik, J.; Mascher, P.; Pusep, Y. A.; Comedi, D.; Guimarães, F. E. G. J. Appl. Phys., 2010, 108, 013105

25. Mastronardi, M. L.; Maier-Flaig, F.; Faulkner, D.; Henderson, E. J.; Kübel, C.; Lemmer, U.; Ozin, G. A. Nano Lett., 2011, 12, 337–342

26. Sun, W.; Qian, C.; Mastronardi, M. L.; Wei, M.; Ozin, G. A. Chem. Commun., 2013, 49, 11361–11363

27. Shaw, S.; Yuan, B.; Tian, X.; Miller, K. J.; Cote, B. M.; Colaux, J. L. Migliori, A.; Panthani, M. G.; Cademartiri, L. Adv. Mater. 2016, 28, 8892-8899

28. Drahi, E.; Blayac, S.; Borbely, A.; Benaben, P. Phys. Status Solidi A 211, 2014, 1301–1307

29. Buchter, B.; Seidel, F.; Fritzsche, R.; Lehmann, D.; Bu¨lz, D.; • Buschbeck, R.; Jakob, A.; Schulze, S.; Freitag, H.; Lang, H.; Hietschold, M.; Zahn, D. R. T.; Mehring, M. J Mater Sci 2015, 50, 6050–6059

30. Hana, L.; Xina, Y.; Liua, H.; Ma, X.; Tang, G. Journal of Hazardous Materials 175 ,2010, 524–531

31. Depla, D.; Colpaert, A.; Eufinger, K.; Segers, A.; Haemers, J.; De Gryse, R. Vacuum 66, 2002, 9–17

32. Birnie, D.P.; J. Mater. Res. 2001, 16, 1145-1154

CHAPTER 4. CONCLUSIONS

Bottom up techniques of nanomaterial synthesis with colloidal nanoparticles provide the scope for a high level of control of material properties by enabling us to control each constituent grain. However, for creating a phase pure inorganic structure, the organic ligands have to be removed. Calcination is one of the most extensively used methods for removing organics from colloidal nanostructure assemblies (CNAs) to obtain an inorganic nanostructured material. In this work, we investigate the effectiveness of calcination in removing carbon from CNAs and compare it with plasma processing, using a model system of colloidal ZrO_2 nanoparticles for the study.

We find that while plasma processing removes the carbon from the organic ligands almost completely, calcination is found to be remarkably ineffective in removing carbon from the CNAs. Even after extreme conditions of calcination of 800^{o}C at 12 hrs almost 18% of the initial carbon is seen to be retained in the CNA thin films. We find that diffusion of oxygen and volatiles do not limit the rate of carbon removal in calcination. We suspect the high amount of carbon retained to be in the form of black carbon, the presence of which causes calcination to result in the formation of a composite structure rather than a phase pure structure, as in case of plasma processing. This remnant carbon may affect the properties of the CNAs in different ways like conductivity, mechanical strength etc. also affects the material's efficiency in different applications (catalysis, sensors). We observe a decreased activation energy of grain growth leading to earlier grain growth in calcined CNAs as compared to plasma processed samples.

As plasma processing is observed to be superior to calcination in carbon removal in CNAs, we then apply plasma processing for removing ligands from Silicon nanoparticle

assemblies to synthesize nc-silicon thin films. We find that the thin films produced have reactive ion etch rates that are comparable but faster than the commercial standard single crystalline silicon. The synthesis of such carbon free silicon nanoparticle thin films can be very valuable for application in the semiconductor industry for making microelectronic/nanoelectronics devices. With an increase in complexity and cost involved in miniaturization of such devices the using top down techniques, bottom up approaches with silicon nanoparticles can offer a solution.